Delft University of Technology
Faculty of Applied Sciences

Bachelor of Science Thesis

Numerical study on the determination of the rheological properties of power-law fluids in the ultrasonic waveguide experiment

Author:
Lotte Borstlap

Supervisor:
Dr. ir. Martin Rohde

Thesis committee:
Dr. ir. Danny Lathouwers
Dr. ir. Martin Rohde

August 17, 2020

TU Delft

Abstract

In this thesis, a method to retrieve the rheological parameters of power-law fluids is examined, for the purpose of gaining more knowledge on the properties of fluids used in the Molten Salt Fast Reactor. The currently researched method to perform this rheological measurement is the ultrasonic waveguide viscometer, in which a wave is sent through a steel waveguide, losing its energy along the way due to viscous dissipation. By measuring the amplitude attenuation due to this energy loss, the viscosity of fluids can be found. This thesis focuses on the question how the rheological properties of power-law fluids can be accurately retrieved from the amplitude measurements in the ultrasonic waveguide viscometer. The used research-method is the development of a numerical model in MATLAB to mimic this experiment. In this way, a data-set of the amplitude-profile on the waveguide is obtained computationally. Subsequently, a method of data-processing that was proposed to retrieve the rheological parameters from this data-set is researched. Through this model, accuracy of the proposed methods are tested, as well as the influence of the rheological properties on this accuracy.

In this thesis, a numerical model to simulate the velocity and amplitude profiles for Newtonian and power-law fluids was developed successfully. In this process, a new method was introduced in order to reduce calculation time and data storage. The viscosities for two Newtonian fluids were retrieved successfully and accurately by using this method. Subsequently, the method was used for power-law fluids. The results on this rheological model were twofold, namely for the power index m and the consistency index K_m. The results on the power index showed to be very accurate for the three tested fluids. On the consistency index, a large deviation on the theoretical values showed. Concluding, the proposed methods for the ultrasonic waveguide viscometer and method of data-processing proved to be very suitable for power index measurements. However, measurements on the consistency index asks for a more accurate or sensitive method.

For further research, it was recommended to examine the sensitivity of the consistency index with respect to the power index. Some methods to do so were proposed. Furthermore, the influence of m and K_m on the required waveguide length is of interest. Gaining knowledge on these two subjects will, expectantly, enable the ultrasonic waveguide experiment to be used for measurements on power-law fluids. Lastly, the developed numerical model can be expanded for other complex rheologies, such as Bingham or Casson fluids.

Contents

Chapter 1

Introduction

Considering the rapid world energy consumption and the resulting fast-pace global warming, the development of sustainable and clean energy sources is now crucial. One solution for this problem lies in the technology of nuclear reactors as a sustainable energy provider. The generation of nuclear energy is regarded to be very promising as no greenhouse gasses are emitted through the process. Moreover, nuclear energy is more efficient and reliable than more conventional sources like solar and wind energy. However, nuclear energy is prone to more popular criticism due to safety considerations. The radioactive waste that is produced in nuclear reactors can cause great damage to the environment, as horrifically demonstrated during nuclear accidents in Chernobyl and Fukushima. These downsides were reason to set up The Generation IV International Forum (GIF) in 2000, with the goal to develop efficient, clean, safe and economically competitive nuclear reactors [1]. One type these generation-IV reactors is the Molten Salt Fast Reactor (MSFR), which design promises to reach high safety and environmental standards. The SAMOFAR project has been set up to perform research on the MFSR, with the goal to prove the innovative safety concepts of the MSFR [2] and ultimately to design the reactor. The Reactor Institute Delft is involved in the SAMOFAR project by researching the fundamental behaviour and properties of the used salt. One of these properties is the viscosity of the fluid, which amongst others, is crucial in the development in the MSFR. This thesis focuses on a method of determining the viscosity of fluids showing complex behaviour, such like molten salts.

1.1 Molten Salt Fast Reactor

In figure 1.1 the design of the MSFR reactor core is shown. It consists of a single cylindrical vessel, filled with a molten fuel salt. A ring of thorium-salt in the walls of the vessel acts as a breeding blanket, transmuting non-fissile thorium-232 to fissile uranium-233 upon capturing a neutron [3]. This process heats up the fuel salt, which moves in upward direction through the central core zone. At the top reach, the molten salt flows downwards through the heat exchangers, releasing its thermal energy. Part of the molten salt exits the loop for reprocessing, such that multiple fission products can be separated. In addition, soluble and gaseous fission products are removed from the salt by injecting gas bubbles at the bottom of the core. Furthermore, a drainage pipe and freeze-plug are shown at the bottom of the core. This freeze-plug is being cooled electrically, ensuring that in the case of an accidental power-shut, the freeze-plug will melt and the molten salt will drain to a fail-safe storage tank [2].

A favourable aspect of the MSFR is the twofold purpose of the molten salt, namely as both fuel and coolant. This means that the conventionally used coolant being water is absent in the MSFR, eliminating steam explosion accidents. Another safety-win lies in the fact no long-lived radioactive waste is produced [4].

Currently, the MSFR is only being studied in computer models. In order to produce a working and safe system, it is necessary to know how the system and its molten salt react in different situations. As mentioned before, it is therefore crucial to measure the physical properties of the

molten salt. One of these crucial properties is the rheological behaviour, providing understanding on the fluid flow of the molten salt in the MSFR. For example, this is necessary to correctly model and design the heat transfer and the flow inside the reactor core. Furthermore, knowledge on the rheological behaviour enables the detailed design of emergency designs, such as the freeze-plug and safety tanks [3].

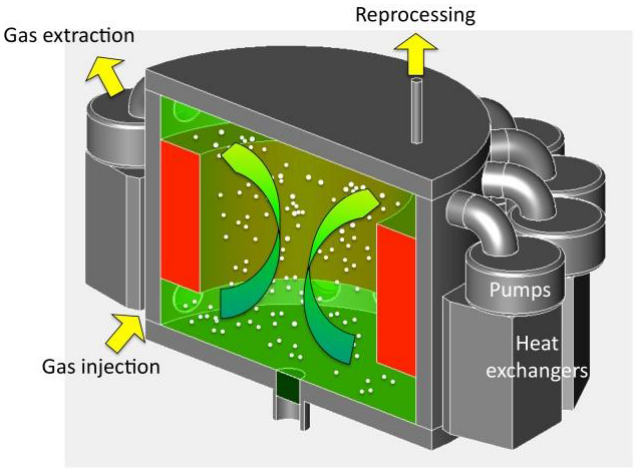

Figure 1.1: Schematic drawing of Molten Salt Fast Reactor [2]

1.2 Determination viscous behaviour

The research performed at the Reactor Institute Delft on the MSFR-design focuses on thorium-cycle in the reactor, which uses thorium in a fluoride salt with the composition LiF-ThF_4-UF_4-PuF_3h as a fuel. Currently, different types of methods are already available for measuring viscous behaviour of molten salts. Significant research on viscometers was performed by Cohen and Jones [5] and later by Cantor [6], both using a modified form of a rotational viscometer [7]. Another technique of a torsional viscometer was developed by Chrenkova [8] and at the Kurchatov institute [9].

However, these two conventional methods mostly work with a larger amount of fluids, while this is undesirable when working with the molten salt due to its high radioactivity. This complex salt shows three other properties which add to the complexity of measuring its viscous behaviour. Firstly, Thorium-salt has a high melting point, around 600 °C [10]. Moreover, previously performed research on this salt [11] [12] predicts the effective viscosity of the salt to be relatively low, approximately 3 $mPas$. Lastly, the salt is highly corrosive. All these properties together disable the use of conventional viscometer set-ups.

The aforementioned issues require the design of a new measurement set-up. Some research proposes the use of acoustics for determining the viscous behaviour at high temperatures, as firstly performed in 1949 by Maston et al [13]. In this research, the use of a transducer is proposed, converting an electrical signal to a mechanical displacement. In Mason's research the transducer is in direct contact with the fluid, which can not withstand the high corrosiveness of the molten salt. Moreover, the Curie temperature of the piezoelements in the transducer is far below the melting point of the used molten salt, causing it to demagnetise. A newer set-up was researched by Vogt, Lowe&Cawley [14], in which the viscous behaviour was measured by ultrasonic guided waves. In this research, a vertical cylindrical waveguide is partly immersed in the fluid, making that the transducer is separated from the salt. From the attenuation of the reflected waves that travel through the immersed waveguide, the viscous behaviour could be measured. This thesis is based on the lastly described method.

Despite of the ultrasonic waveguide viscometer to overcome conventional experimental problems, the technique does give rise some new complexities of its own. These complexities mostly emerge in the data-processing of the amplitude measurements to the concluding rheological properties. Some research has gone into this technique and data-processing to find the viscosity of Newtonian

fluids [7] [3]. This proved to be quite successful, as in such Newtonian fluids the rheology is simple, which makes that an analytical solution to the velocity profile in the fluid is available. In the case of Newtonian fluids, the viscosity can be directly derived from the amplitude-attenuation. However, in practise most fluids, such as molten salts, are suspected *not* to be Newtonian. That is, the fluid movement under shear stress is more complex. This complexity makes that an analytical solution to the amplitude-profile for these non-Newtonian fluids is more complex as well. Therefore, the amplitude attenuation measured with the ultrasonic waveguide method does not straight-forwardly provide the fluid's rheological properties. Some assumptions have to be made in the measurements of these fluids, which could simplify the determination of the rheological properties out of the measured amplitude. Rohde [15] used some of these assumptions to derive an analytical model and data-processing method for a specific type of non-Newtonian fluids, being power-law fluids. Rohde's approach is the starting point of the numerical model composed in this thesis.

1.3 Thesis outline

Considering the probable arising rheological problems in the viscous measurements for non-Newtonian fluids, as described in the previous section, the research of the compatibility of the ultrasonic waveguide viscometer for non-Newtonian fluids is of interest. This research focuses on power-law fluids, a specific type of non-Newtonian fluid. This gives rise to the general research question:

- How can the rheological properties for power-law fluids be accurately retrieved from the amplitude measurements in the ultrasonic waveguide viscometer?

Some experimental measurements with the ultrasonic viscometer set-up were performed on power-law fluids at TU Delft. However, the set-up showed not to be sensitive enough to accurately measure the small amplitude attenuation shown by power-law fluids. This gave rise to the interest of simulating the experiment by computational means, from which more accurate data can be retrieved. Rohde [15] proposed a method of retrieving the viscosity out of the amplitude data, which can be tested by the computational method. This leads to the main research question of this thesis:

- How can the analytically derived method by Rohde be used in the measurement of the rheological properties of power-law fluids with the ultrasonic waveguide viscometer? And what is influence of the rheological properties on the accuracy of this method?

To reach this goal, a numerical experiment to mimic the ultrasonic viscometer for power-law fluids will be developed in MATLAB. First the numerical model is developed for Newtonian fluids. The velocity profile in the fluid is simulated by using the discretized Navier-Stokes equations. Then, the viscous dissipation and resulting amplitude attenuation in a plate geometry will be modelled, and the dynamic viscosity can be retrieved. These simulations are used to benchmark our numerical model. Subsequently, the model is expanded for power-law fluids, using the solution for the amplitude profile analytically derived by Rohde [15]. By linear data-fitting the effective viscosity of the modelled power-law fluids can be retrieved. This method will be applied to a range of power-law fluids for which rheological constants are known from earlier studies.

The resulting model of the numerical study can be used in further experimental research on the ultrasonic viscometer, to directly perform the data-processing. Another application of the results of this thesis is to optimize ultrasonic viscometer set-up.

Firstly, the theory background of the experiment is described in chapter 2. This chapter elaborates on the phenomenon of shear stress and different rheologies, as well as on the set-up of the ultrasonic waveguide viscometer and its energy balance. In chapter 3 the numerical method in described. This consists of a derivation of the numerical governing equations, as well as a detailed description of the composed MATLAB-code. Subsequently, chapter 4 describes the results of the numerical model, which include the velocity profiles, amplitude profiles and (effective) viscosity values for some different fluids. This chapter also includes a discussion about the composed MATLAB model and its results. Lastly, chapter 5 gives the conclusions of this thesis and recommendations for further research.

Chapter 2

Theoretical background

In this chapter, the relevant theory for this research will be discussed. Firstly including the theory behind shear stress and non-Newtonian fluids. After that, the ultrasonic waveguide set-up will be introduced from which the analytical amplitude profile will be derived using an energy balance.

2.1 Shear stress and rheology

In figure 2.1 a stationairy laminar fluid flow in the x-direction is depicted. In this example, v_x is stationary and a function of the y-coordinate, $v_x = v_x(y)$. The layer of fluid directly under the plane $y = y_1$ has a larger velocity than the layer directly above it. Therefore, one can imagine the lower layer to exert a friction force on the above control volume $dxdy$. As the friction force is proportional and parallel to the surface A it acts on, the force is not classified as pressure, but rather a *shear stress* τ_{yx} $[Pa]$ [16].

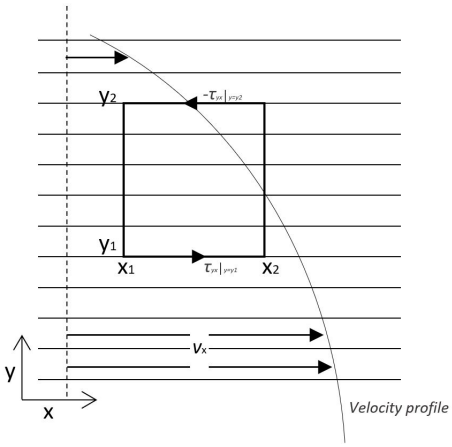

Figure 2.1: Control volume $dxdy$ in a stationary, laminar fluid flow. Friction forces are exerted on the control volume $dxdy$, the so-called *shear stress* τ_{yx}.

The description of the relation between shear stress and the local velocity gradient is called the *rheology* [16]. Based on different rheological relations, all fluids can be categorized into Newtonian and non-Newtonian fluids.

2.1.1 Newtonian fluids

The most simple rheological model is *Newton's law*, in which the shear stress is proportional to the velocity gradient [16]:

$$\tau_{yx} = -\mu \frac{dv_x}{dy}, \tag{2.1}$$

with τ_{yx} the shear stress $[Pa]$, μ the dynamic viscosity $[Pas]$ and v_x the velocity in x-direction $[ms^{-1}]$. Furthermore, dv_x/dy is often referred to as the *shear rate* $\dot{\gamma}$ $[s^{-1}]$.

Fluids that satisfy Newton's law are called *Newtonian fluids*. Unfortunately only a small amount of fluids (somewhat) satisfy this model. Examples of some Newtonian fluids are water, air and some glycerol-mixtures.

2.1.2 Power-law fluids

Most fluids display non-Newtonian behaviour, that is the shear stress is not directly proportional to the velocity gradient. Non-Newtonian fluids can be categorized into different rheologic models. Perhaps the most common non-Newtonian fluid-model is given by the *Ostwald-De Waele* or the *power-law* model [16]:

$$\tau_{yx} = -K_m \left| \frac{dv_x}{dy} \right|^{m-1} \cdot \frac{dv_x}{dy}, \tag{2.2}$$

in which K_m is called the *consistency index* $[Pas^m]$ and m the *flow index* $[-]$. These two parameters will be referred to as the *rheological parameters* of a power-law fluid.

The parameter m subdivides fluids into *pseudo-plastics* or *shear-thinning* fluids when $m < 1$ and *dilatant* or *shear-thickening* fluids when $m > 1$. Examples of shear-thinning fluids are apple sauce and cream, tomato juice and cornstarch are shear-thickening fluids. Note that the extreme case in which $m = 1$, the power-law model refers to Newtonian behaviour. For the case of $m = 0$, the power-law model indicates plastic or solid behaviour [17]. A major drawback of the power-law model is that it predicts an infinite viscosity (when $m < 1$) as the shear rate tends to zero. However, the actual viscosity of power-law fluids has a finite and constant value at very low shear rates [17].

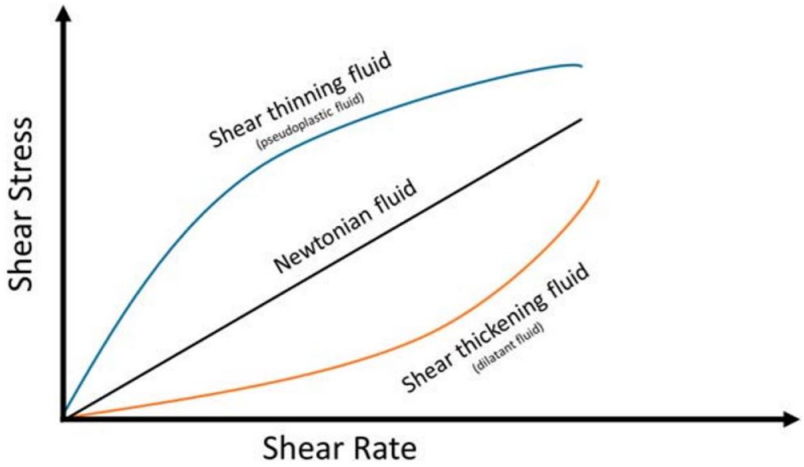

Figure 2.2: Schematisation of shear stress-shear strain plot for Newtonian and Non-Newtonian power-law fluids [18]

In the case of non-Newtonian fluids, one refers to the *effective viscosity* μ_{eff} rather than just the viscosity. In figure 2.2 the shear stress as a function of the shear rate is plotted, in which the effective viscosity is represented by the slope of the line. The varying slope illustrates that, in contrast to the viscosity for Newtonian fluids, the effective viscosity for fluids with $m \neq 1$ is not a constant but depends on the local shear rate. The dependence of the effective viscosity on the shear rate can be observed from the formula of the effective viscosity for power-law fluids as well, which is retrieved from equation 2.2 and given by:

$$\mu_{eff} = K_m \cdot \left| \frac{dv_x}{dy} \right|^{m-1}. \tag{2.3}$$

2.2 Ultrasonic waveguide experiment

The basic idea of the ultrasonic waveguide viscometer is to generate sinusoidal shear waves by a transducer and to lead these waves through a waveguide, illustrated in figure 2.3. In this case, the waveguide is a stainless steel plate, through which the waves travel with velocity c_s. At the plate's surface, the waves exert a shear stress on the immersion fluid, initiating a local velocity profile in the fluid. In this way the shear wave loses energy at the guide's surface, a process called *viscous dissipation*. Due to the viscous dissipation, the returning waves have a reduced amplitude, which is referred to as *amplitude attenuation*. The rate of energy energy loss in the shear wave, and thus in its amplitude, is a measure of the viscosity of the surrounding fluid.

This section briefly describes the theory of shear waves. Subsequently, a derivation of the relation between the amplitude attenuation and the fluid's (effective) viscosity is proposed.

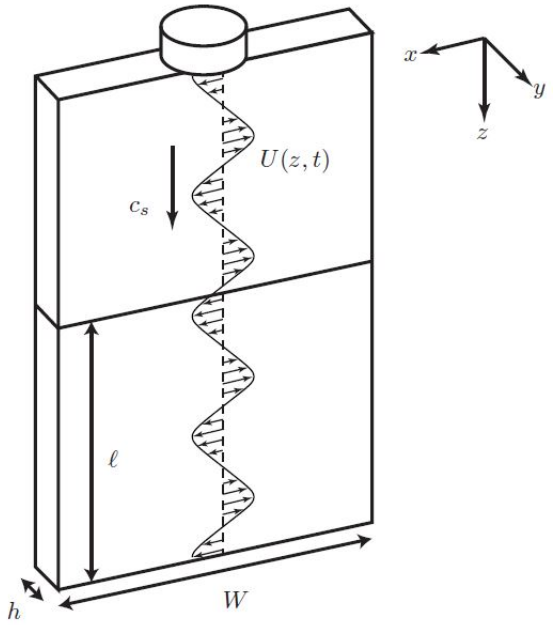

Figure 2.3: Schematic drawing of the waveguide with thickness h and width W, party immersed in the molten salt over length l. A representation of the shear waves initiated by the transducer with form $u(z,t)$ is illustrated [15].

2.2.1 Shear waves

In general, two wave modes can be present in a plate: *longitudinal* and *shear* wave modes. These modes all correspond to different polarization directions of a wave. With the coordinates of the plate being defined in figure 2.3, longitudinal waves are polarized in the z-direction and shear waves in the x-direction. In this set-up, shear waves are used as these modes are nondispersive and have the advantage to attribute their amplitude attenuation merely to the viscous effect of the fluid [7].

2.2.2 Power loss due to viscous dissipation

In this section the energy balance of the waveguide will be constructed, from which a differential equation for the amplitude can be stated. For Newtonian fluids the differential equation can be solved analytically. An analytical solution will be derived for the power-law fluids, based on some approximations. This section is based on an internal paper by Rohde [15].

The shear waves that are initiated at the top of the waveguide, and travel in the z-direction have the form:

$$u(z,t) = A(z)\sin(kz - \omega t), \tag{2.4}$$

in which $A(z)$ is the amplitude along the length of the waveguide $[m]$, $k = 2\pi/\lambda$ the wavenumber $[m^{-1}]$ and ω the angular frequency $[s^{-1}]$. The local plate velocity in the x-direction can now be

written as

$$v_x(z,t) = \frac{du(z,t)}{dt} = -A(z)\omega\cos(kz-\omega t) = B(z)\cos(kz-\omega t), \tag{2.5}$$

in which $B(z) = -\omega A(z)$ is the velocity amplitude $[ms^{-1}]$.

The main interest is the loss of energy of the sinusoidal shear waves at the guide's surface, for which an mechanical energy balance of a fraction dz of the waveguide can be composed. It is assumed that the energy loss at the sides of the plate, the two (y,z)-planes, can be neglected as $h/W << 1$. Now the balance for wave energy is given as

$$hWdz\frac{de_w}{dt}(z,t) = P(z,t) - P(z+dz,t) + \Delta P_\tau(z,t), \tag{2.6}$$

in which e_w is the wave energy density $[Jm^{-3}]$, P the wave power that is transmitted along the waveguide in the z-direction $[Js^{-1}]$ and P_τ the energy lost by shear friction $[Js^{-1}]$. The power loss term is due to shear stress τ_0 acting on the surface Wdz, on both sides of the plate. The loss term can now be described as:

$$\Delta P_\tau(z,t) = -2\tau_0(z,t)\cdot v_x(z,t)\cdot W\cdot dz. \tag{2.7}$$

For the purpose of measuring the viscosity, the time-averaged attenuation of the shear wave along the direction of the shear wave is of interest. Therefore the energy equation 2.6 is integrated over one period T. For the spatial power derivative the integration gives the following simplification:

$$\frac{1}{T}\int_T -\frac{1}{W}\frac{P(z+dz,t)-P(z,t)}{dz} = \frac{1}{T}\int_T -\frac{d}{dz}P'(z,t)dt = -\frac{d}{dz}\left(\frac{1}{T}\int_T P'(z)\right) = \frac{d}{dz}\tilde{P}'(z). \tag{2.8}$$

The time-averaged integration of the time-derivative of e_w becomes zero:

$$\frac{1}{T}\int_T h\frac{d}{dt}e_w(z,t)dt = 0. \tag{2.9}$$

The zero-term can be explained by looking at this wave energy integration in the *Eulerian* frame, instead of in the *Langrangian* frame. These frames indicate two different ways of looking at a fluid motion. In a Eulerian frame, one focuses on a specific location in space through which the fluid flows as time passes, whereas in a Langrangian frame the observer follows an individual fluid parcel as it moves through space and time. The different frames can be easily visualized by respectively sitting on a bank and watching a river flow by, or sitting on a boat and drifting down a river [19]. Notice that in this energy equation the Eulerian frame is regarded, as the passing wave is observed from a volume element $hWdz$ at the waveguide. In this volume element, all lost energy to viscous dissipation is originating from the wave energy. That is, no accumulation of energy can take place in the volume element, proving the statement in 2.9.

Substituting 2.7, 2.8 and 2.9 into 2.6 and rewriting yields the following energy equation:

$$\frac{d}{dz}\tilde{P}'(z,t) = -2\tau_0(z,t)v_x(y=0,z,t). \tag{2.10}$$

In the end, the amplitude attenuation is of interest. Therefore the energy equation is stated in terms of $B(z)$, by using the following description of $\tilde{P}'(z)$ [15]:

$$\tilde{P}'(z) = \frac{1}{2}h\rho_s c_s B(z)^2, \tag{2.11}$$

in which c_s marks the wave velocity in the plate $[ms^{-1}]$, ρ_s the density of the waveguide's material $[kgm^{-3}]$ and h the thickness of the plate $[m]$. Now the final energy equation is obtained, in terms of the velocity amplitude $B(z)$:

$$B(z)\frac{dB(z)}{dz} = -\frac{1}{\rho_s c_s h}\frac{1}{T}\int_T 2\tau_0(z,t)v_{x,0}(z,t)dt. \tag{2.12}$$

No further general description can be given for the remaining loss term, as it is dependent on the rheology of the fluid. Therefore this loss term will be separately derived for two different rheologies, being Newtonian fluids an power-law fluids.

Analytical solution for Newtonian fluids

To further derive an analytical solution for the amplitude profile $B(z)$, a description of the velocity profile v_x has to be found. The solution to Stoke's second problem is used for this velocity profile. This problem describes the motion of a in-compressible fluid caused by the sinusoidal oscillation of an *entire* flat plate. For Newtonian fluids, Stoke's second problem can be solved analytically [20], giving the solution for the velocity profile in the fluid given in 2.13:

$$v_x(y,z,t) = B(z)e^{-y/\delta}\cos(\omega t - y/\delta), \tag{2.13}$$

in which δ is the viscous skin depth (m), described as:

$$\delta = \left(\frac{2\mu}{\omega\rho_f}\right)^{1/2}. \tag{2.14}$$

However, in the set-up of the ultrasonic viscometer, Stoke's second does not apply in principle, as not the *entire* plate oscillates sinusoidally. That is, $dv_x/dz \neq 0$ close to the plate's surface. However, as $\delta \sim \mu m << \lambda \sim mm$, the velocity gradient in the z-direction has an insignificant influence:

$$\frac{dv_x}{dy} \approx \frac{v_x}{\delta} \qquad \text{and} \qquad \frac{dv_x}{dz} \approx \frac{v_x}{\lambda} \qquad \Longrightarrow \qquad \frac{dv_x}{dy} >> \frac{dv_x}{dz}. \tag{2.15}$$

Therefore it can be assumed that the solution for the velocity profile in a Newtonian fluid can safely be approximated by equation 2.13. Using equation 2.13 and Newton's law in equation 2.1, it can be derived that the time-averaged term on the right side of 2.12 equals

$$-\frac{1}{T}\int_T 2\tau_0 v_{x,0}(z,t)dt = -\frac{\mu}{\delta}B(z)^2. \tag{2.16}$$

The mechanical energy equation 2.12 can therefore be rewritten in terms of the amplitude $B(z)$:

$$\frac{dB(z)}{dz} = -\frac{\mu}{\delta\rho_s c_s h}B(z), \tag{2.17}$$

giving the analytical solution for the velocity amplitude $B(z)$ for Newtonian fluids in terms of the viscosity of the fluid:

$$B(z) = B_0 exp\Big(-\frac{\mu}{\delta\rho_s c_s h}\cdot z\Big) = B_0 exp(\alpha\cdot z), \tag{2.18}$$

in which B_0 $[ms^{-1}]$ represents the initial amplitude of the shear wave at $z = 0$.

Analytical solution for power-law fluids

For power-law fluids, an analytical solution for $B(z)$ to equation 2.12 is of interest as well. Unfortunately, in contrast to Newtonian fluids, no analytical solution to Stoke's second problem for power-law fluids is available. To enable an approximation of v_x in the fluid, an assumption based on Ai&Vafai [17] is used. In this paper, Stoke's second problem was numerically solved for power-law fluids for different values of power index m. It was found that the flow behaviour index m is of insignificant influence on the velocity gradient at the plate's surface $y = 0$. Making that it can be safely assumed that for power-law fluids $\dot{\gamma}_0 = \dot{\gamma}_{0,N}$. Using this assumption, the time-averaged term on the right side of equation 2.12 for power-law fluids can be derived [15], giving:

$$-\frac{1}{T}\int_T 2\tau_0 v_{x,0}(z,t)dt = -K_m\Big(\frac{B(z)\sqrt{(2)}}{\delta}\Big)^m B(z)P_3(m), \tag{2.19}$$

in which the viscous skin depth is defined as $\delta = (2K_m/\omega\rho_f)^{1/2}$, with $K_1 = \mu$, and $P_3(m)$ is a polynomial approximation:

$$P_3(m) - 0.00630863m^3 + 0.0399466m^2 - 0.129211m + 0.448619. \tag{2.20}$$

Substituting 2.14 and 2.19 into 2.12 and rearranging gives the final differential equation for amplitude $B(z)$ for power-law fluids:

$$\frac{dB(z)}{dz} = -\frac{\sqrt{2}P_3(m)}{h}\left(\frac{2\omega^m\rho_f^m K_m^{2-m}}{\rho_s^2 c_s^2}\right)^{1/2} B(z)^m = \alpha_m B(z)^m. \tag{2.21}$$

Solving this differential equation gives an approximation for the velocity amplitude $B(z)$ for power-law fluids, in terms of the rheological parameters K_m and m:

$$B(z) = \left(B_0^{1-m} + (1-m)\alpha_m z\right)^{1/1-m} \tag{2.22}$$

2.2.3 Navier-Stokes equations

In order to avoid incorporating assumptions and approximations in the numerical computations with respect to the velocity profile in the fluid, the *Navier-Stokes equations* are used. One form of the set of Navier-Stokes equations describes the time-dependent three-dimensional flow of incompressible fluids, given as [16]:

$$\rho\frac{\partial \boldsymbol{v}}{\partial t} = -\rho\boldsymbol{v}\cdot\boldsymbol{\nabla}\boldsymbol{v} - \boldsymbol{\nabla}\cdot\boldsymbol{\tau} - \nabla p + \rho\boldsymbol{g}, \tag{2.23}$$

in which ρ is the density of the fluid $[kgm^{-3}]$, $\boldsymbol{v}$ the velocity vector $[ms^{-1}]$, $\boldsymbol{\tau}$ the shear stress tensor $[Pa]$, p the pressure $[Pa]$ and $\boldsymbol{g}$ the gravity vector $[ms^{-2}]$.

In the set-up of the ultrasonic viscometer, the Navier-Stokes equations can be simplified. Many terms cancel out when using the following principles specific to the situation described in figure 2.3:

1. no pressure gradient and gravity effects play a role in the fluid, thus $\boldsymbol{\nabla}p \approx 0$ and $\boldsymbol{g} = 0$;
2. the initiated wave has an amplitude in the x-direction, thus $v_y = v_z = 0$;
3. no convection occurs, hence $\boldsymbol{v}\cdot\boldsymbol{\nabla}\boldsymbol{v}$;
4. all shear stresses are zero, except for $\tau_{yx}(y)$.

Using these four statements into equation 2.23 gives the following equation, specific for this ultrasonic waveguide experiment:

$$\frac{\partial v_x}{\partial t} = -\frac{1}{\rho_f}\frac{\partial \tau_{yx}}{\partial y}. \tag{2.24}$$

Equation 2.24 gives the solution for the velocity profile in the fluid. At the boundary $y = 0$, velocity profile in the fluid meets with the one in the plate. The latter being derived in the previous section. The boundary condition for the velocity at $y = 0$ is given as:

$$v_x(y = 0, z, t) = B(z)\cos(kz - \omega t). \tag{2.25}$$

In the experimental method, the implementation of formula 2.24 in a numerical script will be further discussed.

Chapter 3

Numerical method

The method of research in this numerical study, is to develop a model that determines the rheological properties of a power-law fluid, based on its velocity profile in the fluid in concurrence with the wave energy in the plate. Hence numerically mimicking measurements performed by the ultrasonic waveguide experiment.

This numerical model is set up by firstly using a 1D-approach in which the velocity profile for $v_x(y)$ in the y-plane is determined for one value of of z. From this, the shear stress τ_{yx} was calculated using the rheology of the fluid. After this 1D-approach, this technique is extrapolated for a larger range of z on the plate, giving data on the attenuation of the amplitude of the wave. The acquired data on $B(z)$ is then processed and fitted in order to find the rheological properties of the fluid. This method of modelling is firstly performed for a Newtonian fluid, as a benchmark of the code. After that, a power-law rheology is applied to the model.

Furthermore, new parameters X and I_X are introduced to make the derivations more convenient and the code faster. In section 3.1, X and I_X are derived. In section 3.2 the non-dimensional formulation of all relevant parameters is given. Next, all used differential equations are discretized in section 3.3. In section 3.4 the techniques of data-processing and fitting for the sake of retrieving the viscosity from the 'measured' data is explained. Lastly, section 3.5 presents code by means of two flow diagrams.

3.1 Introduction of X and I_X

For further derivations, it is important to notice that $B(z)$ can be treated as a scaling factor for v_x and τ_{yx}. For example, equation 2.5 shows that $v_x \sim B(z)$ and similarly the power-law rheology in equation 2.2 shows that $\tau_{yx,PL} \sim B(z)^m$. It turns out to be convenient in the numerical calculations to treat the amplitude $B(z)$ this way. That is, to factor out $B(z)$ of the velocity and shear stress, which is done by introducing the quantity $X(z,t)$ $[kg \cdot s^{(m-2)} \cdot m^{(1-m)}]$:

$$X(z,t) = \frac{1}{B(z)^{m+1}} \cdot \tau_0(z,t) v_{x,0}(z,t). \tag{3.1}$$

Note that $X(z,t)$ is expected to be a periodic function, as both v_x and τ_{yx} are periodic as well. Moreover, note that the z-dependence of $X(z,t)$ resides in the shifting of the periodic function over t, for different values of z. That is, this z-dependence is *not* referring to an amplitude reduction as a function of z, as this reducing $B(z)$ has just been factored out. The convenience of using $X(z,t)$ can be illustrated when being substituted in the differential energy equation 2.12:

$$B(z)\frac{dB(z)}{dz} = -\frac{1}{\rho_s c_s h}\frac{2}{T}\int_T B(z)^{m+1} X(z,t)dt = -\frac{1}{\rho_s c_s h}\frac{2}{T} B(z)^{m+1}\int_T X(z,t)dt. \tag{3.2}$$

Equation 3.2 shows that the out-factoring of $B(z)$ by introducing $X(z,t)$ results in an integral which is independent of the amplitude. This simplifies further calculations, as the integral can be

calculated for all values of z, independent of the amplitude attenuation. That is, the calculation of v_x and τ_{yx} does not require iteration for the reducing $B(z)$ as a result of viscous dissipation. Note that integrating $X(z,t)$ over one period T gives the same value *for every* z, as this is a sinusoidal function around 0. The quantity I_X is introduced to represent the time-averaged integral of X:

$$I_X(z) = \frac{2}{T}\int_T X(z,t)dt. \tag{3.3}$$

In this definition $I_X(z) = \text{constant}$. In other words, $I_x \neq f(z)$. This can be explained by the fact that the z-dependence is only referring to a shift of the periodic signal over t at different values of z. If the periodic $X(z,t)$ is integrated over one period T, this will thus give the same value regardless of what z-coordinate is given. Substituting I_X into equation 3.2 and rearranging leaves the final differential equation for the calculation of amplitude $B(z)$:

$$\frac{dB(z)}{dz} = -B(z)^m \cdot \frac{I_X}{\rho_s c_s h}. \tag{3.4}$$

Using equation 3.4, I_X can be calculated for one value of z (for example, z_0) directly out of one calculation of $X(z = z_0, t)$. In other words, no iteration for every Δz is required in the calculation of the power-loss term, reducing the complexity of the MATLAB script and the calculation time.

3.2 Non-dimensional formulation

The technique of *non-dimensionalization* is often applied to differential equations. It refers to the removal of physical dimensions in an equation, by introducing a suitable substitution of variables. By applying a non-dimensional mathematical model, no physical quantities need to be assigned. This approach is a simplification of great convenience, as one simulation will then be valid for many types of fluids. Also, this non-dimensional approach increases the understanding of the physical problem [21].

3.2.1 Derivation non-dimensional quantities

The following non-dimensional quantities are introduced, defined by Ai&Vafai [17] and D.Pritchard [22]. Here $\hat{a}$ marks the non-dimensionalized variable a.

$$\hat{v_x} = \frac{v_x}{v_0}, \tag{3.5}$$

$$\hat{t} = \omega \cdot t, \tag{3.6}$$

$$\hat{y} = \left(\frac{\omega}{\nu_0 v_0^{m-1}}\right)^{\frac{1}{m+1}} \cdot y, \tag{3.7}$$

$$\hat{z} = \frac{z}{z_{tot}}, \tag{3.8}$$

in which v_0 $[ms^{-1}]$ is the reference velocity at $y = 0$, ω $[s^{-1}]$ the frequency of the vibration, ν_0 $[m^2s^{-1}]$ the reference kinematic viscosity of a Newtonian fluid, m the flow index and z_{tot} $[m]$ the total length of the waveguide. These four non-dimensional quantities are used to non-dimensionalize the shear stress τ_{yx} and the parameter $\hat{I}_{\hat{X}}$.

Substituting $\hat{v}_x$ and $\hat{y}$ into the power-law rheology 2.2 gives

$$\tau_{yx,PL} = -K_m\left(\frac{\omega}{\nu_0 v_0^{m-1}}\right)^{m/(m+1)} \cdot \left|\frac{d\hat{v}_x}{d\hat{y}}\right|^{m-1}\frac{d\hat{v}_x}{d\hat{y}}, \tag{3.9}$$

yielding the non-dimensionalized shear stress for power-law fluids $\hat{\tau}_{yx,PL}$

$$\hat{\tau}_{yx,PL} = {K_m}^{-1}\left(\frac{\omega}{\nu_0 v_o^{m-1}}\right)^{-m/(m+1)} v_0^{-m} \cdot \tau_{yx,PL}. \tag{3.10}$$

For completeness, the non-dimensional parameter $\hat{\tau}_{yx}$ is written out for the special case of $m = 1$, thus a Newtonian fluid. The substitution $K_1 = \mu$ was used, as well as $\nu_0 = \mu_0/\rho_f$. This substitution turns out to be convenient, as for Newtonian fluids $\mu/\mu_0 = 1$. Substituting into equation 3.10 gives

$$\hat{\tau}_{yx,N} = \mu^{-1}\left(\frac{\omega}{\nu_0}\right)^{-1/2} v_0^{-1} \cdot \tau_{yx} = (\omega\nu_0)^{-\frac{1}{2}}(v_0\rho_f)^{-1} \cdot \tau_{yx}. \tag{3.11}$$

In order to obtain $\hat{I}_{\hat{X}}$, $\hat{B}$ and $\hat{z}$ are substituted into equation 3.4:

$$\frac{v_0\hat{B}(\hat{z})}{d\hat{z}} = \frac{1}{\rho_s c_s h} v_0^m \hat{B}(\hat{z}) \cdot \hat{I}_{\hat{X}}. \tag{3.12}$$

By doing some rearranging, $\hat{I}_{\hat{X}}$ becomes[1]:

$$\hat{I}_{\hat{X}} = \frac{1}{\rho_s c_s h z_{tot}} v_0^{m-1} \cdot I_X. \tag{3.13}$$

3.2.2 Non-dimensional set of equations

This section gives all relevant equations stated in terms of the now derived non-dimensional quantities. Substituting $\hat{v}_x$, $\hat{t}$, $\hat{\tau}_{yx}$ and $\hat{y}$ into the Navier-Stokes equation 2.24 gives the corresponding non-dimensional equation:

$$\frac{\partial\hat{v}_x}{\partial\hat{t}} = -\frac{\partial\hat{\tau}_{yx}}{\partial\hat{y}}. \tag{3.14}$$

The general non-dimensional formulation of the shear stress of a power-law fluid 2.2 as a function of the power-index m is given in the following equation The convenience of the definition of $\hat{y}$ in 3.7 is clearly demonstrated, as all constants cancel out:

$$\hat{\tau}_{yx,PL} = -\left|\frac{d\hat{v}_x}{d\hat{y}}\right|^{m-1}\frac{d\hat{v}_x}{d\hat{y}}. \tag{3.15}$$

For the special case of a Newtonian fluid $m = 1$, this equation reduces to:

$$\hat{\tau}_{yx,N} = -\frac{d\hat{v}_x}{d\hat{y}}. \tag{3.16}$$

Furthermore, $\hat{X}$ and $\hat{I}_{\hat{X}}$ are defined as follows:

$$\hat{X} = \frac{1}{\hat{B}(\hat{z})} \cdot \hat{\tau}_{yx,0}\hat{v}_{x,0}, \tag{3.17}$$

$$\hat{I}_{\hat{X}} = \frac{2}{\hat{T}}\int_{\hat{T}} \hat{X}(\hat{z},\hat{t})d\hat{t}. \tag{3.18}$$

Lastly, the non-dimensional formulation of the differential equation for amplitude attenuation 3.4 is defined as[2]:

$$\frac{\hat{B}(\hat{z})}{d\hat{z}} = -\hat{B}(\hat{z})^m \cdot \hat{I}_{\hat{X}}. \tag{3.19}$$

3.3 Discrete formulation

The *discretization* of a function $f(x)$ refers to the segmentation of the continuous function into data points $[x_i, f_i]$. This process is illustrated in figure 3.1. Discretization is needed to be able to solve differential equations numerically. Several methods are available for the numerical approximation of differential equations. Some of those methods are defined as finite difference approximations, such as the *forward finite difference*, the *backward finite difference*, the *central finite difference* and the *Crank-Nicolson* schemes [24]. In this research, the forward finite difference and central finite difference model are utilized.

[1] Many different derivations of the non-dimensional parameters can be composed. In appendix 6.1, an alternative derivation is given.

[2] This non-dimensional formulation of $\hat{B}$ is not completely in line with the definition of $\hat{I}_{\hat{X}}$. Appendix 6.1 elaborates on this finding.

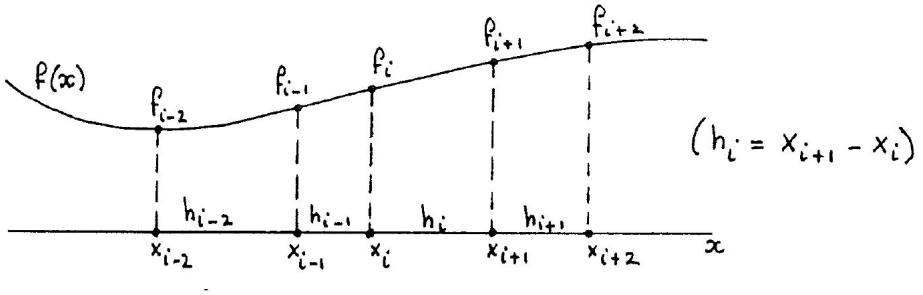

Figure 3.1: Illustration of the discretization of continuous function $f(x)$ into a discrete data set of points $[x_i, f_i]$. [23]

3.3.1 Discrete differentiation and integration

Generally, the most accurate first-order differential approach is the central linear approximation, which for equidistant intervals $h_i = h_{i-1} = h$ is given by [23]:

$$f'(x_i) \approx \frac{f_{i+1} - f_{i-1}}{2h}. \tag{3.20}$$

Some calculations in this research requir the evaluation of a function $f'(x)$ in $x = 0$, for which a central differential approach proves to be unsuitable. In those cases, a second order forward difference approach was used [23]:

$$f'(x_i) \approx \frac{-3f_i + 4f_{i+1} - f_{i+2}}{2h}. \tag{3.21}$$

The partial derivatives in time were discretized by a first order forward difference approximation. This approximation is given by [23]:

$$f'(t_n) \approx \frac{f_{n+1} - f_n}{\Delta t}. \tag{3.22}$$

The time-averaged integral I_X was approached numerically using the *trapeziodal method*. In this approximation the interpolating function is a straight line between points $(t_\mathrm{n}, f_\mathrm{n})$ and $(t_\mathrm{n+1}, f_\mathrm{n+1})$, making that the discrete integration of $f(t)$ at the interval $[a = t_{n=1}, b = t_{n=N_t}]$:

$$\int_a^b f(t)dt \approx \sum_{n=2}^{N_t} \frac{f_{n-1} + f_n}{2} \Delta t. \tag{3.23}$$

3.3.2 Discrete set of equations

This section aims to determine discrete forms for the governing equations in the numerical model, with the idea of replacing the derivatives in those equations by the defined approximations in section 3.3.

This section describes the discretization for all *dimensional* governing equations (2.1, 2.2, 2.24, 3.3, 3.4). The corresponding *non-dimensional* equations - given in section 3.2.2 - were of course discretized as well, in the exact same way. Furthermore, for convenience in writing, this section uses v to refer to v_x, as well as τ for τ_{yx}.

The finite difference approach involves both the time and spatial derivatives to be replaced by finite differences. The following notation of the numerical approximation is used to do this:

$$a^n_{i,k} \approx a(y_i, z_k, t_n), \qquad \text{where} \qquad t_n = n\Delta t, \qquad y_i = i\Delta y, \qquad z_k = k\Delta z. \tag{3.24}$$

Different schemes are available to approach the partial differential Navier-Stokes equation and rheology equation. In this research an explicit approach was used, rather than an implicit one.

Despite of the explicit scheme having the ability to become unstable, it is the easier to implement in MATLAB and the less numerically intensive [24].

The Navier-Stokes equation 2.24 is discretized by using a forward time central space (FCTS) [24]. That is, the equation is discretized in time by using the forward scheme in equation 3.22 and discretized in space by using a central approach given in equation 3.20. Yielding the discrete Navier-Stokes equation as follows:

$$v_{i,k}^{n+1} = v_{i,k}^{n} - \frac{1}{\rho_f}\frac{\Delta t}{2\Delta y}\Big(\tau_{i+1,k}^{n} - \tau_{i-1,k}^{n}\Big). \tag{3.25}$$

The availability of a boundary condition for $v_x(y = 0)$ at the plate's surface enables the use of this central approach. That is, equation 3.25 can be computed starting from $y_{i=1}$. This is not the case for the rheology equations 2.1 and 2.2, as no specific boundary condition for $\tau_{yx}(y = 0)$ is available. In this case the forward approach has to be used. By doing so, the following discrete shear-stress equations for power-law are retrieved:

$$\tau_{i,k}^{n} = -\frac{K_m}{(2\Delta y)^m}\big|-3v_{i,k}^{n} + 4v_{i+1,k}^{n} - v_{i+2,k}\big|^{m-1}\Big(-3v_{i,k}^{n} + 4v_{i+1,k}^{n} - v_{i+2,k}^{n}\Big) \tag{3.26}$$

In which the discrete shear-rate is defined as:

$$\dot{\gamma}_{i,k}^{n} = (-3v_{i,k}^{n} + 4v_{i+1,k}^{n} - v_{i+2,k}^{n})/(2\Delta y) \tag{3.27}$$

Note that for the case $\dot{\gamma}_{i,k}^{n} > 0$, equation 3.26 simplifies to

$$\tau_{i,k}^{n} = -K_m\left(\frac{-3v_{i,k}^{n} + 4v_{i+1,k}^{n} - v_{i+2,k}^{n}}{2\Delta y}\right)^m = -K_m\Big(\dot{\gamma}_{i,k}^{n}\Big)^m \tag{3.28}$$

And similarly, for the case $\dot{\gamma}_{i,k}^{n} < 0$

$$\tau_{i,k}^{n} = K_m\left(-\frac{-3v_{i,k}^{n} + 4v_{i+1,k}^{n} - v_{i+2,k}^{n}}{2\Delta y}\right)^m = K_m\Big(-\dot{\gamma}_{i,k}^{n}\Big)^m \tag{3.29}$$

The constant integral I_X 3.3 is described by using a the discrete approximation given in 3.23:

$$I_X = \frac{2}{T}\sum_{n=1}^{N_n-1}\frac{\Delta t}{2}\big(X_{i=1,k}^{n} + X_{i=1,k}^{n+1}\big) \tag{3.30}$$

Lastly the differential equation describing the amplitude profile 3.4 is discretized using a first order forward approach in z-space:

$$B_{i=1,k+1}^{n} = (B_{i=1,k}^{n})^m - \frac{1}{\rho_s c_s h}2\Delta z \cdot B_{i=1,k}^{n} \cdot I_X \tag{3.31}$$

3.4 Data-processing: determination of the rheological properties

When the numerical MATLAB model has computed the amplitude profile $B(z)$, the first part of the computation is completed. At that point, the ultrasonic waveguide experiment has been mimicked numerically. These computed data is expected to be much more accurate than those of a physical measurement, due to the absence of, sometimes significant, experimental uncertainties.

In this section, the methods to retrieve the rheological properties m and K_m from this computed $[z, B]$-datasets are described. This thesis applies these methods to the computationally obtained data-set, but note that these methods can applied to physically measured amplitude profiles as well. The data-processing differs for Newtonian and power-law fluids, whose corresponding methods are described in section 3.4.1 and 3.4.2, respectively.

In this research, the viscosity of Newtonian fluids is computed by the numerical model first. By performing these computations, the MATLAB code can be benchmarked: if the correct viscosities are retrieved it can be concluded that the velocity profiles and amplitude attenuation are calculated correctly. The viscosity of two Newtonian fluids are computed by the numerical model - both non-dimensional as dimensional, which is described in section 3.4.1. After this, the amplitude computations were performed for power-law fluids. From this the rheological parameters m and K_m for power-law fluids could be retrieved. The method to do so is described in section 3.4.2.

3.4.1 Newtonian fluids

Note that the amplitude-profile for Newtonian fluids is expected to show an exponential decay, as was shown in equation 2.18. Using the data-set $[z, B]$ the amplitude-profile $B(z)$ is fitted to an exponential function $C1 * exp(C2 \cdot z)$ using a MATLAB fit-function, in which $C2 = \alpha_{fit}$. The MATLAB-fit of the exponent has standard confidence bounds of 95%. The fit was performed for the both non-dimensional and dimensional amplitude profiles $\hat{B}(\hat{z})$ and $B(z)$.

Non-dimensional

From the non-dimensionally derived $\hat{\alpha}_{fit}$, the viscosity μ can be calculated as follows:

$$\mu = \hat{\alpha}_{fit}^2 \cdot 2\rho_f \nu_0. \tag{3.32}$$

The derivation of equation 3.32 is given in appendix **??**. Note that this method of finding μ is inapplicable in physical experiments, as the values of ρ_f and ν_0 are required to know beforehand. Nevertheless, if the right values of μ are retrieved, this method can confirm the correctness of the non-dimensional calculation of the velocity and amplitude profiles.

Dimensional

To retrieve the viscosity μ from the dimensional data, the attenuation constant α_{fit} from the exponential decay of the dimensional $B(z)$ profile is used. The viscosity is found by using the analytical solution to the ampltiude profile stated in equation 2.18 and the formulation of δ in 2.14, giving:

$$\mu = \alpha_{fit}^2 \cdot \frac{2\rho_s^2 c_s^2 h^2}{\omega \rho_f}. \tag{3.33}$$

3.4.2 Power-law fluids

After the benchmark of the method for Newtonian fluids, the numerical model is used for the calculation of the rheological properties K_m and m of power-law fluids. This computation is more complicated, as *two* constants have to be retrieved and thus fitted to the amplitude profile. Moreover, the analytical solution for $B(z)$ for power-law fluids in equation 2.22 is more complicated.

Rohde [15] proposed a method in his report in which m and K_m can be found by fitting the measured data set (z, B) to a linear function, obtained from equation 2.22

$$\Delta B^* = K_m \cdot \Delta z^*, \tag{3.34}$$

in which

$$\Delta B^*(z) = \left| B(z)^{1-m} - B_0^{1-m} \right|^{2/(2-m)}, \tag{3.35}$$

$$\Delta z^* = \left[\frac{2P_3(m)}{\rho_s c_s h} |1-m| (\omega \rho_f)^{1/2} \cdot z \right]^{2/(2-m)}. \tag{3.36}$$

In this way only m needs to be varied to find the slope K_m with the smallest fit error.

The fitting is performed by methods of a manual minimization problem. That is, $\Delta B^*(m_{fit})$ and $\Delta z^*(m_{fit})$ are calculated with the given data set of (z, B) for a range of m_{fit}-values: $m_{fit} = [0.1, 1.8]$, with $\Delta m = 1.7/400 = 0.00425$. With mm being the index of m_{fit}, thus $m_{fit,mm} = mm\Delta m$. The obtained data-sets for $[\Delta B^*(z), \Delta z^*]$ for 400 different values of m_{fit} is visualized in figure 3.2, for the example of soybean oil.

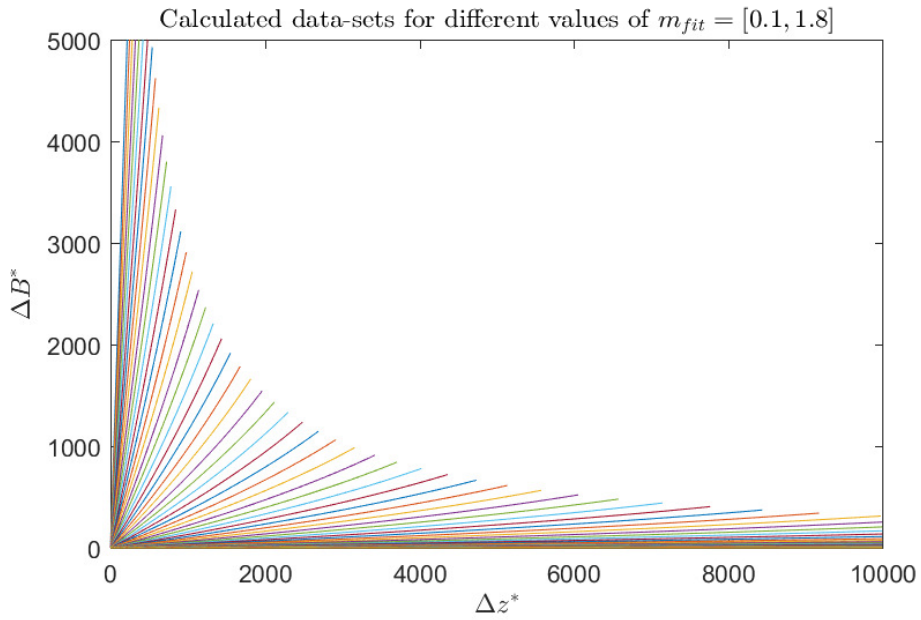

Figure 3.2: Plots of manipulated data-set $[\Delta B^*, \Delta z^*]$ by means of equations 3.35 and 3.36 for $m_{fit} = [0.1, 1.8]$. Note that not all values m_{fit} result in a linear function.

Out of all the different data-sets $[\Delta B^*(z), \Delta z^*]$ for different values of m_{fit}, the one that fits a linear function the nearest is of interest. As this is the value of m_{fit} that should correspond to the measured fluid, according to the linear method in 3.34. As can be seen in figure **??**, some calculated data-sets $[\Delta B^*(z), \Delta z^*]$ somewhat approach a linear function, but it can not be observed directly which one does the most accurately. To find the best linear fit $[\Delta z^*, \Delta B^*]$ is fitted to a linear function for every value of m_{fit}, by the POLYFIT1 function of MATLAB. This fit plots a function $y_{fit} = p1 \cdot \Delta z^* + p2$ to the data-set. Thus a number of mm different fitted functions are calculated. Out of this set of fits, the best linear fit to the measured data of $B(z)$ was found by minimizing the total error in y_{fit}, being:

$$\epsilon_{y_{fit}}(m_{fit}) = \sum_{k=1}^{N_z} \sqrt{\Big(y_{fit}(z, m_{fit}) - \Delta B^*(z, m_{fit})\Big)^2}, \tag{3.37}$$

such that m can be found at $\epsilon_{y_{fit}}(m_{fit}) \to 0$ and the corresponding value of K_m at the same m_{fit}-index for the slope $p1(mm)$.

3.5 MATLAB code

In this section, the MATLAB code of this research is described in more detail. The used constants and boundary conditions for the dimensional calculations are given in section 3.5.1. Also, the stability conditions for the used intervals of variables y, t and z are discussed in 3.5.2. Lastly, the complete MATLAB model is described in the form of two flow diagrams in section 3.5.5.

3.5.1 Constants

Some constants require to be defined as they arise in the dimensional governing equations. In the research of Rook [7] the ultrasonic waveguide experiment was physically performed. All relevant constants were measured, which are given in table 3.1.

Different fluids were mimicked by the numerical model, whose rheological parameters are given in table 3.2.

Quantity	$c_s\ [ms^{-1}]$	$h\ [m]$	$\rho_s\ [kgm^{-3}]$	$f\ [Hz]$	$z_{tot}\ [m]$	$v_0\ [ms^{-1}]$
Value	3083	$202{\cdot}10^{-6}$	7876	$3{\cdot}10^{-3}$	$203.5{\cdot}10^{-3}$	$80{\cdot}10^{-3}\cdot\omega$

Table 3.1: Experimental constants. In which c_s is the wave velocity, h the thickness of the plate, ρ_s the density of the stainless steel waveguide, f the frequency of the incident wave, z_{tot} the total length of the plate, v_0 the initial shear wave speed (amplitude) [7] [15].

Fluid $[kgm^{-3}]$	**Power index** $m\ [-]$	**Consistency index** $K_m\ [Pas^m]$	**Density** ρ_f
Water	1	0.0001	997
Air	1	$18.3{\cdot}10^{-6}$	1.185
Tomato ketchup	0.3	6.47	1136
Soybean oil	0.51	2.18	930
Ethylene glycol	1.29	0.0011	1110

Table 3.2: Rheological constants for different fluids. The values for water and air where retrieved from [25], ketchup from [26], soybean from [27] and ethylene glycol from [28]. Newtonian fluids are marked by $m = 1$, for which $K_1 = \mu$.

3.5.2 Boundary conditions

The fluid surrounding the waveguide is at rest at $t = 0s$. At time $t = 0^+$ the sinusoidal wave is initiated at the top of the plate, and the plate's transmits the motion into the fluid. The boundary and initial conditions in discrete form are given by:

$$v_{i,k}^{n=1} = 0 \qquad \text{for} \qquad y_i > 0 \tag{3.38}$$

$$v_{i=1,k}^{n} = \sin\Big(kz_k - t_n\Big) \qquad \text{for} \qquad t_n > 0 \tag{3.39}$$

$$v_{i,k}^{n} \to 0 \qquad \text{for} \qquad y_i \to \infty \tag{3.40}$$

$$B_{k=1}^{n} = v_0 \tag{3.41}$$

Note that in equation 3.39, amplitude $B(z)$ has been factored out. All calculations in the code of $v_x(y)$ were performed with this unit amplitude, as was described in section 3.1.

3.5.3 Stability conditions

In the numerical model it is of great importance to implement the right Δz, Δy and Δt. This is to ensure the stability of the differential computational schemes, as well as to minimize uncertainties in the calculations. Although smaller intervals mostly account for more accurate results, the limited data storage and run-time of the script have to be be taken into consideration.

The FCTS scheme in equation 3.25 can produce unstable solutions that oscillate and grow if Δt is too large [24]. Stable solutions with the FTCS scheme are only obtained if[3] [29]

$$\frac{1}{\rho_f}\frac{\Delta t}{\Delta y^2} \leq \frac{1}{2} \tag{3.42}$$

By trial-and-error, the maximum required Δt was found at $\Delta t = 2\pi/8000\omega$. This time-step was used in all calculations, on an interval of $t = [0, 3\pi/\omega]$. No smaller Δt was possible in these calculations, as that would required the Δy to be smaller as well, exceeding the maximum storage.

Concerning y, a rough indication of the necessary length of the y-interval was found in the report of Ai&Vafai [17] to be $\hat{y} = 5$. Using the non-dimensional formulation in 3.7 for $m = 1$, this

[3] As a matter of fact, this stability was derived for Newtonian fluids only. This can be seen by substituting discrete equation 3.26 for $m = 1$ into discrete NS-equation 3.25. Following this derivation, the stability criterion $\Delta t/\rho_f \Delta y^{m+1} < 1/2$ should hold for power-law fluids. However, this criterion proved not to be accurate during the velocity computations. Therefore the Newtonian stability criterion was used as a starting point, for which sometimes some adjustments in Δy had to be made. Some further mathematical research could go into this stability issue.

corresponds to $y \approx 5 \cdot 2.3079 \cdot 10^{-7}$ $[m]$ in dimensional y-space. No boundary condition was assigned at $v_x(y \to \infty)$, requiring to run the script for a long enough y for the velocity profile to approach zero. This minimum run-length of y differs for different fluids with m and K_m and thus will be discussed in the individual calculations. Δy was subsequently determined, based on the stability condition in 3.42.

3.5.4 Visualisation numerical set-up

In order to further visualize the numerical set-up at the waveguide and in the fluid, the boundary conditions and variable-indexing are schematically showed in figure 3.3.

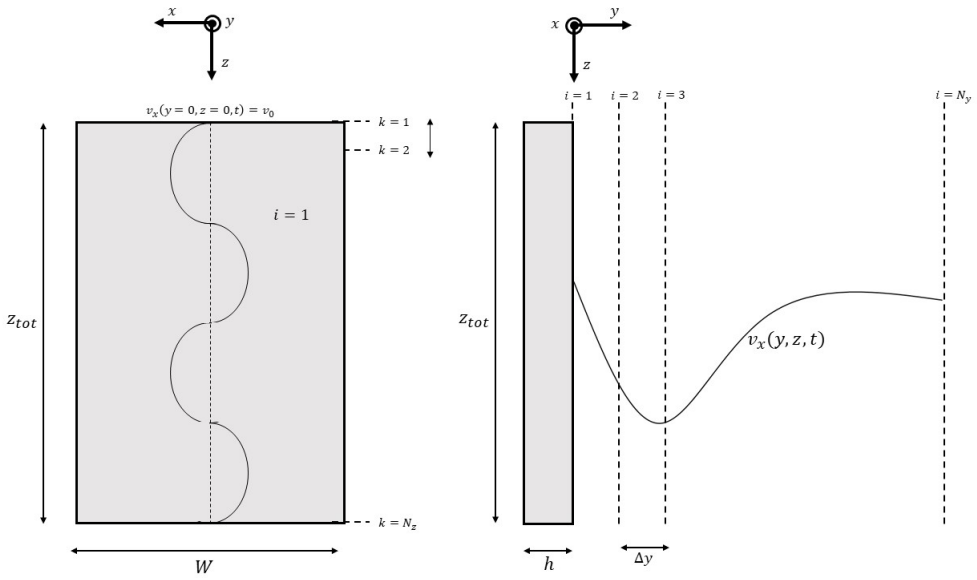

Figure 3.3: Schematic drawing of waveguide in numerical set-up.

3.5.5 Flow-diagrams script

In this section, the composed MATLAB code is depicted in detail by means of two flow diagrams. Basically, these two flow diagrams give a summary of this chapter on the numerical method.

In the first flow diagram, the numerical model for the calculation of the amplitude attenuation in the plate is illustrated. In short, the boundary conditions and experimental constants are inserted, together with the specific rheological constants of the fluid, yielding an amplitude profile $[z, B]$ in the end of the calculations. This is the so-called 'measurement'.

In the second flow diagram, the retrievement of the rheological constants from the measurement is depicted. As seen in previous sections, a different script has to be run for a fluid being a Newtonian or power-law fluid. The retrieved data-set $[z, B]$ from the first flow-diagram is used to retrieve m and K_m through methods of fitting. Note that this part of the code can be used in further *experimental* research as well.

Note that the models are described in terms of dimensional quantities and equations, as the dimensional space is most relevant for the (effective) viscosity determination. As described previously, the non-dimensional model is used as well for benchmarking properties. The same numerical model is used for all corresponding non-dimensional equations.

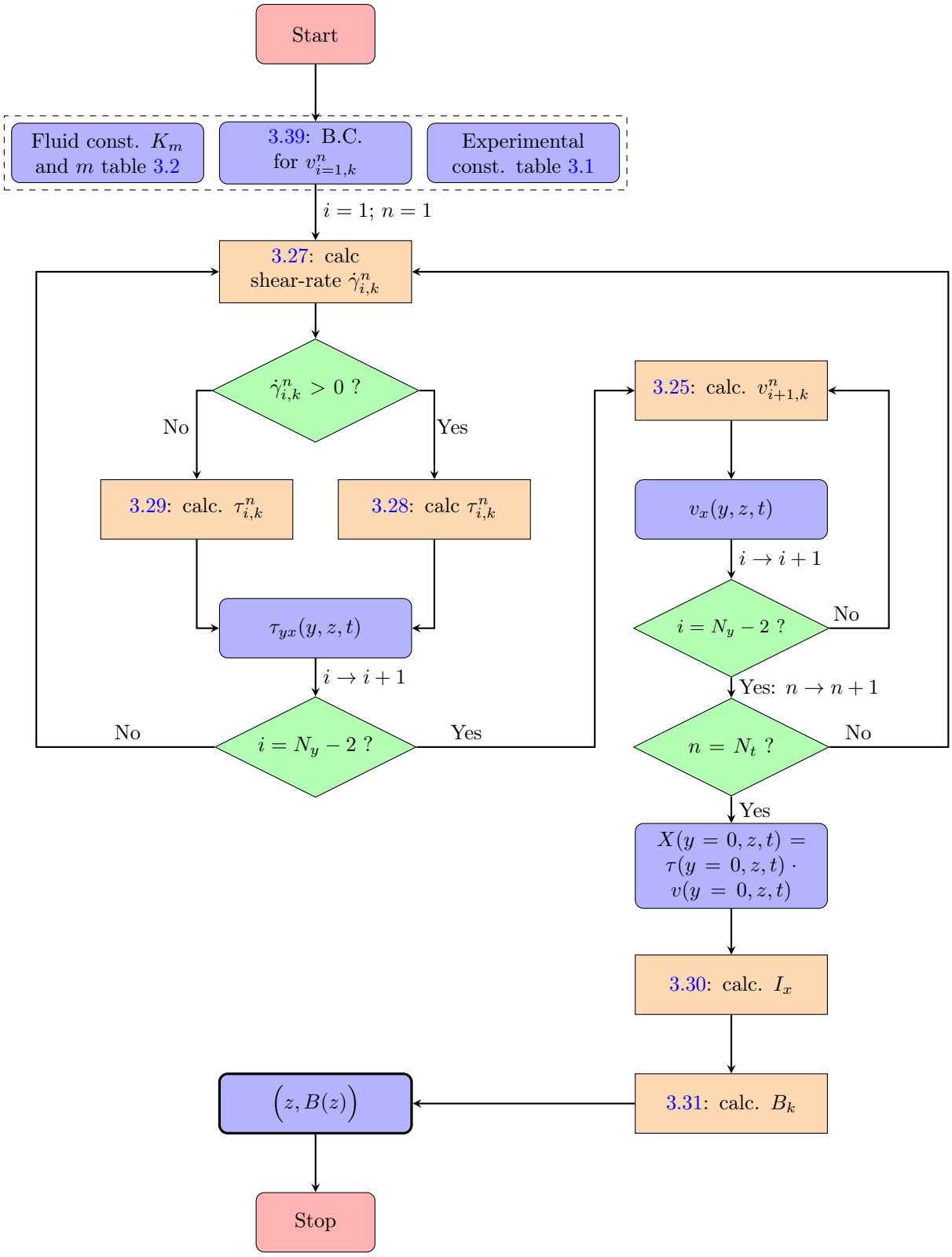

Figure 3.4: Flow-diagram of composed MATLAB-code to mimic the ultrasonic wave-guide experiment, with the amplitude profile $B(z)$ as the outcome.

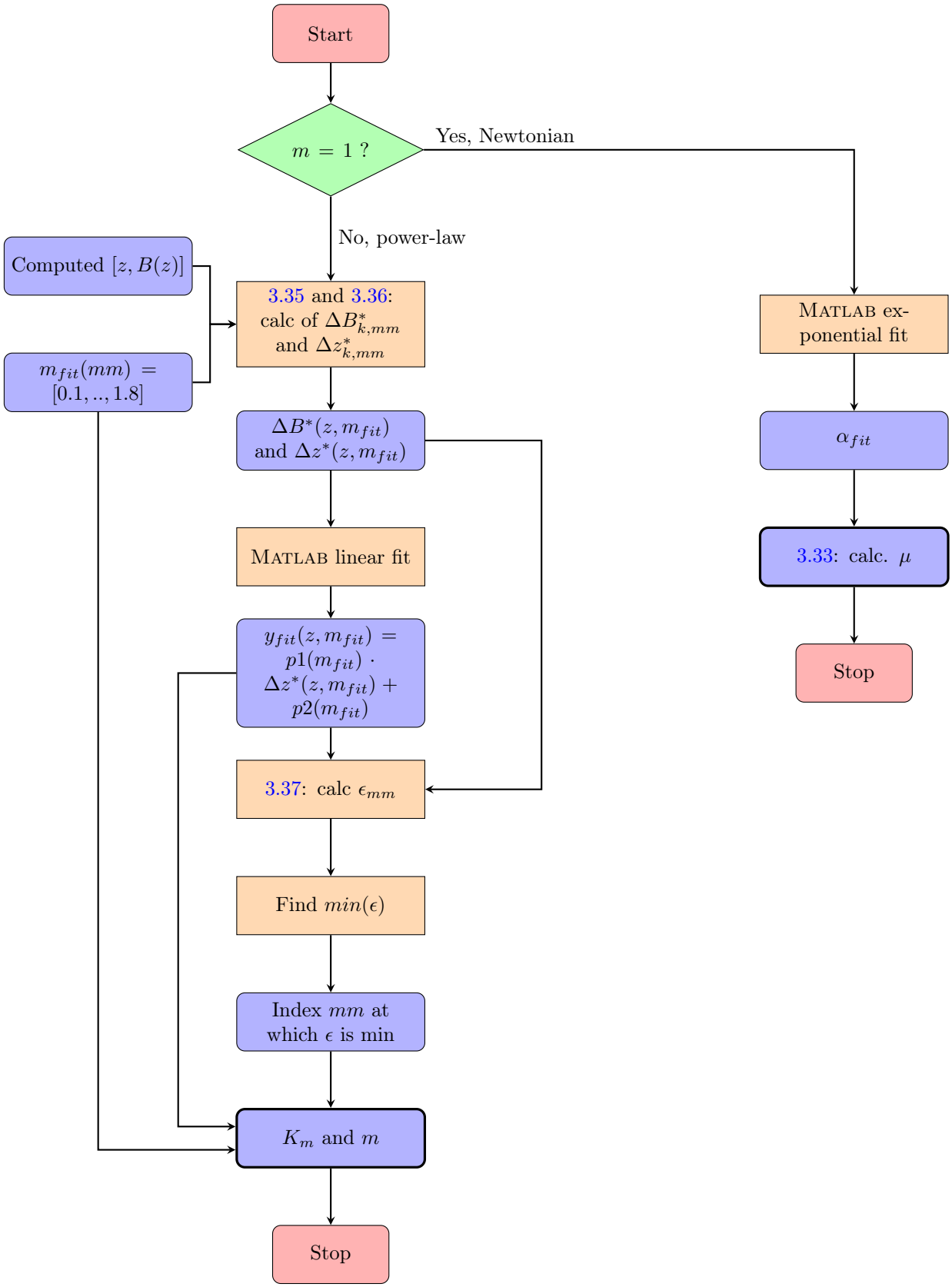

Figure 3.5: Flow-diagram of MATLAB-code for retrieving the rheological parameters from the computed dataset $[z, B(z)]$

Chapter 4

Results and discussion

In this chapter, the results of the computational research are presented, accompanied by discussion about these results. Firstly, the results of the computed velocity profiles of some Newtonian and power-law fluids are given in section 4.1. Section 4.2 showcases the amplitude attenuation due to viscous dissipation for different fluids, plotted both non-dimensionally and dimensionally. Additionally, this section elaborates on the effective viscosity of different power-law fluids and its effect on the minimally required length of the waveguide. In section 4.3 the resulting viscosities of two Newtonian fluids which were computed by the MATLAB script are shown. Lastly, section 4.4 presents and discusses the results on K_m and m for different power-law fluids.

4.1 Velocity profiles

First, the results on the velocity profiles of Newtonian fluids will be presented as they served as benchmarkes for the composed script. After this, the velocity profiles for power-law fluids are shown.

Note that for all calculations the used dimensional time-variable for was $t = [0, 3\pi/\omega]$ and $\Delta t = 2\pi/8000\omega$ as described in section 3.5.3. The corresponding non-dimensional time-variable was $\hat{t} = [0, 3\pi]$ with $\Delta\hat{t} = 2\pi/8000$, based on the non-dimensional formulation in section 3.2.1. The variable Δy differed per calculation, as described in section 3.5.3.

4.1.1 Newtonian fluids

In figure 4.1, the computed non-dimensional velocity profile $\hat{v}_x(\hat{y}, \hat{t})$ in the Newtonian fluid surrounding the waveguide is depicted. For Newtonian fluids, $\hat{y} = [0, 15]$ was found to be the minimal length in order to allow $\hat{v}_x(\hat{y} \to \infty) = 0$. Regarding the stability criterion in equation 3.42, this required $\Delta\hat{y} = 0.1$. The results of Ai&Vafai [17] were used to benchmark the computed velocity profiles. In their paper, the non-dimensional velocity profile for different fluids for incident signal $\hat{v}_x(\hat{y} = 0) = \sin(\omega\hat{t})$ was numerically computed as well. As can be observed, the computed data matches with the literature values, from which it can be concluded that the numerical model for the velocity profile in this thesis is accurate.

Based on this verification, it can be safely assumed that the same numerical procedure can be applied to the *dimensional* velocity profile. In figure 4.2 the results on the dimensional velocity profile for two Newtonian fluids are depicted. The used y-values were $y = [0, 15 \cdot (\nu_0/\omega)]$ with $\Delta y = 0.1 \cdot (\nu_0/\omega)$, based on the previously defined $\hat{y}$ and the non-dimensional formulation in equation 3.7. The dimensional plots show a greater viscous skin for air than for water, which is due to the term μ/ρ_f (see equation 2.14).

Unfortunately, no literature data was found to benchmark the specific dimensional velocity profiles for water and air. Nevertheless, the only manipulations regarding the Newtonian non-dimensional velocity profile to obtaining the dimensional one, were to multiply with well-known constants (μ, ν_0,

ω). Therefore it can be safely concluded that this dimensional velocity profiles for the Newtonian fluids are accurate and correct as well.

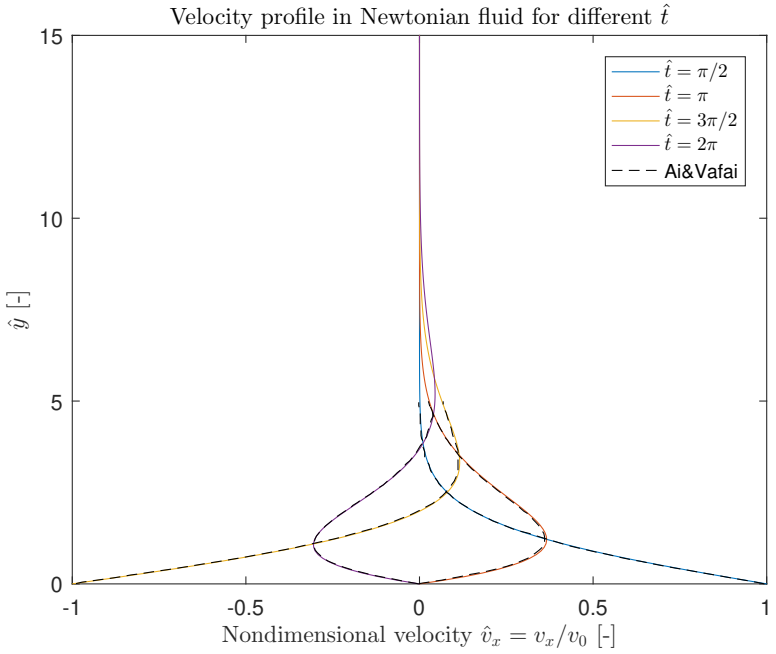

Figure 4.1: Non-dimensional plot of the velocity profile $\hat{v}_x$ as a function of $\hat{y}$, compared with the literature values from Ai&Vafai [17], at different times $\hat{t}$. Note that the literature values are only given up to $\hat{y} = 5$

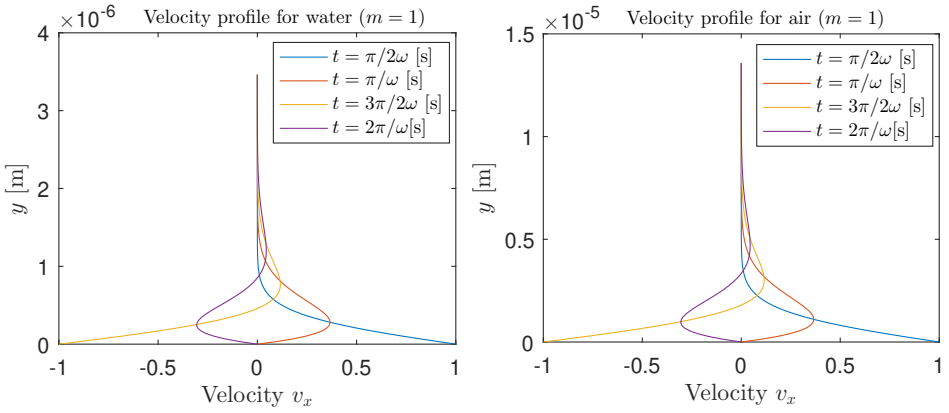

Figure 4.2: Dimensional plots of velocity profile $\hat{v}_x$ as a function of y, for different times t, for two Newtonian fluids. With $\mu_{water} = 0.0001$, $\mu_{air} = 18.4e-6$ $[Pas]$.

4.1.2 Power-law fluids

For power-law fluids, the non-dimensional velocity profile was computed with the script described in the flow-chart (section 3.5.5), in which the influence of m was incorporated. The results for the non-dimensional velocity profiles for theoretical power-law fluids with $m = 0.5$, $m = 1$ and $m = 1.5$ are depicted in subplot 4.3(a). In subplot 4.3(b), (c) and (d), the results are compared to the literature values from Ai&Vafai [17] for $m = 0.5$, $m = 1$ and $m = 1.5$, respectively.

It was found that the viscous skin depth δ was greater for the shear-thinning ($m < 1$) fluids than for shear-thickening. Hence the $\hat{y}$-interval was enlarged to $\hat{y} = [0, 40]$. For stability purposes, described in equation 3.42, Δy was set at $\hat{y} = 0.2$.

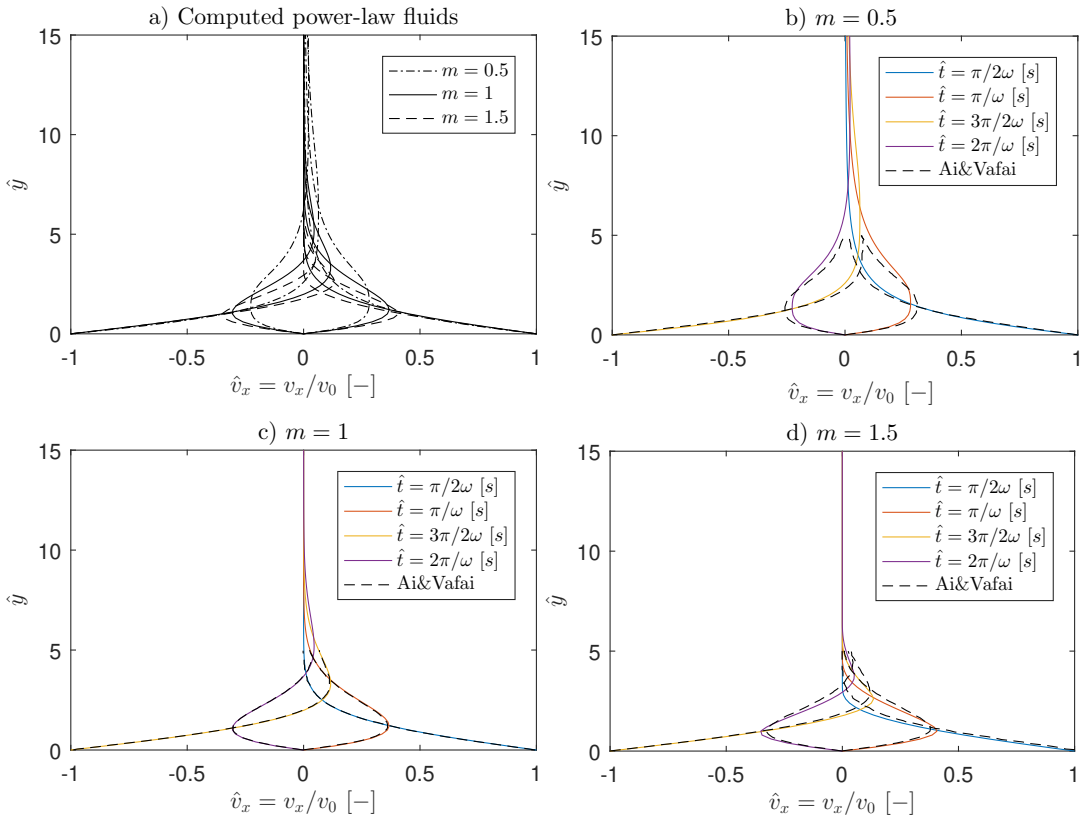

Figure 4.3: Snapshot plots of the non-dimensional profile velocity profile $\hat{v}_x$ for different power-law fluids, as a function of $\hat{y}$. (a) depicts the computed profiles for $m = 0.5$, $m = 1$ and $m = 1.5$. (b),(c) and (d) compare the computed velocity profiles with the corresponding literature values from Ai&Vafai [17] Note that the literature values were only given up to $\hat{y} = 5$.

Note that figure 4.3(c) is computed via the power-law script in which $m = 1$ is inserted, while in the calculation for figure 4.2 the numerical model was simplified beforehand by using $m = 1$. This was done to verify the numerical model for power-law fluids. This indeed indicates a correct application of the script on power-law fluids, as the velocity profile in figure 4.3(c) is still the same as the literature values from for $m = 1$.

Although the dimensionless velocity profiles for $m = 0.5$ and $m = 1.5$ show the same form as the literature data from Ai& Vafai, it does not correspond exactly. A notable observation is that the velocity profile for $m = 0.5$ deviates more from the literature values then for $m = 1.5$. This can be explained by the presumption that the velocity gradients for shear-thinning fluids close to the waveguide's surface are very large compared to the ones for shear-thickening, making it more assumable that numerical faults slip in.

A probable reason for the overall deviation of the computed results could be that Ai&Vafai use a different non-dimensionalisation for $\hat{y}$ than stated in this thesis (see equation 3.7). This makes that the $\hat{y}$-axis could experience a scaling difference compared to the literature values. Unfortunately, it is not straightforward to resolve this scaling problem. The re-scaling of the $\hat{y}$-axis of this research would have to be performed with:

$$\hat{y}_{literature} = \left(\frac{\omega}{\nu_0}\right)^{(m-1)/(2m+2)} v_0^{(m-1)/(m+1)} \cdot \hat{y}_{research} \tag{4.1}$$

Note that this is inconvenient for comparative research, as the $\hat{y}$-axis would be scaled differently for different values of m. Another problem in this scaling lies in the fact that Ai&Vafai's research does not mention the used values for ν_0, ω and v_0. Lastly, it is even more inconvenient to adapt

the definition of $\hat{y}$ from Ai&Vafai, as this does not give the nicely stated non-dimensional equation for $\hat{\tau}$ as described in equation 3.10, independent of all fluid constants. After all, it is assumed that the deviation with respect to the literature values is predominantly caused by this difference in non-dimensional formulation. Hence the velocity profile can be safely used in this research' further calculations of the rheology, as long as the stated non-dimensional formulations are used consequently. This assumption is based as well on the fact that the calculated velocity profile of the Newtonian fluid matches perfectly with the literature values, indicating the numerical correctness of the script.

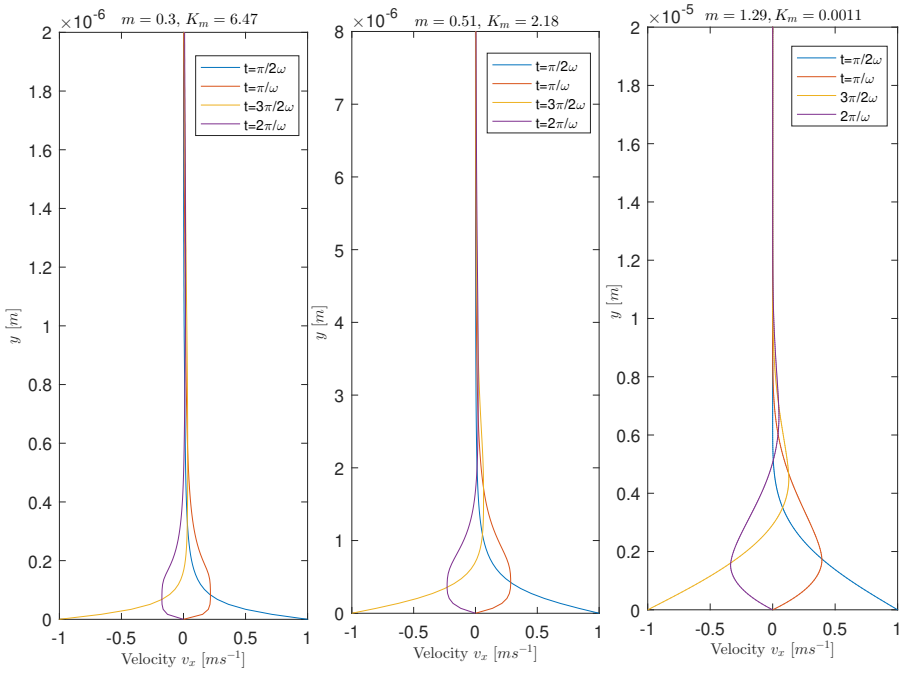

Figure 4.4: Dimensional plots of dimensional velocity profiles power-fluids as a function of y. For the fluids (from left to right): ketchup, soybean oil, ethylene-glycol.

In figure 4.4 the results for the dimensional velocity profiles for three power-law fluids are given. Next to the earlier observed influence of m, the consistency index K_m affects the shape of the velocity profile. For the non-dimensional velocity profiles it was found that the viscous skin depth δ was greater for shear-thinning fluids. However, in dimensional space this is definitely not a rule of thumb, as the viscous skin depth is obviously dependent on K_m as well. Figure 4.4 gives an illustration of this dependence. Ketchup has a smaller m than soybean oil, thus, based on the non-dimensional research, is expected to have a larger viscous skin depth. However, as a result of its larger K_m the viscous skin depth shows to be smaller. It therefore is hypothesized that the viscous skin depth increases with smaller m ánd smaller K_m. This has to be further research, in which ρ_f plays a role in the viscous skin depth as well.

4.2 Amplitude attenuation

With the results on the velocity profiles, the amplitude profile $B(z)$ in the plate can be calculated. In this section the results on this amplitude attenuation for different fluids are shown, both non-dimensionally and dimensionally. Additionally, the minimal required plate's length in the experimental set-up will be discussed.

The used value Δz was different per fluid, as the required wave plate length z_{end} varied heavily - even up to a factor 1000. $N_z = 1001$ was used in all calculations, as this proved to give stable and accurate results. The individual values of z_{end} - and thus Δz - can be retrieved from the given plots in this section.

4.2.1 Newtonian fluids

The amplitude attenuation for two Newtonian fluids as a function of position at the plate z is shown in figure 4.5. The amplitude curve $B(z)$ shows an exponential decay, as was expected by equation 2.18.

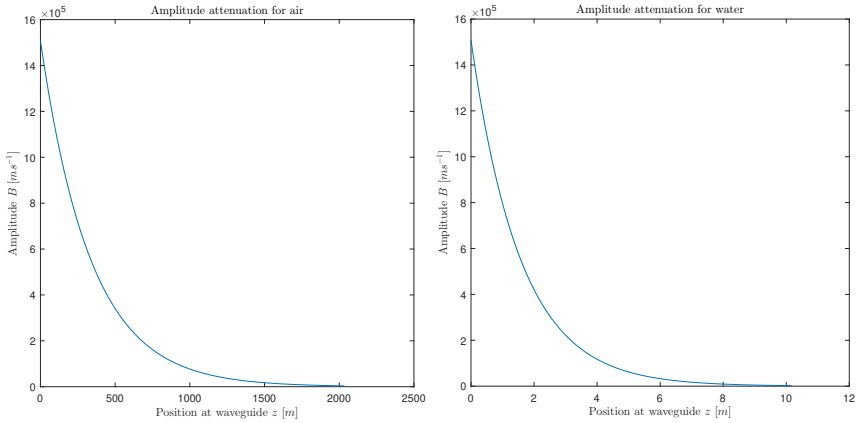

Figure 4.5: Plots of dimensional amplitude profile $B(z)$ for two Newtonian fluids, showing an exponential amplitude attenuation. Note that the calculations have been performed for extreme lengths. The total length of the waveguide in the experiment is much smaller, being $z = 204\ mm$.

It can be observed that the amplitude-decay is steeper for water. This was expected, as water has a larger dynamic viscosity and thus accounts for a larger amount of viscous dissipation, enlarging the amplitude attenuation. Despite of water showing a steeper amplitude-decay, the exponential form starts to show far above the total length of the waveguide, which is $z_{tot} = 204mm$. Nonetheless this proved not to be problematic in the experimental viscosity determination of Newtonian fluids, as has been shown by Rook [7]. In his thesis it was proved that there is an unique exponent that can be fitted to the typical exponential amplitude decay shown by a Newtonian fluid, even for small immersion depths.

4.2.2 Power-law fluids

The results on the non-dimensional amplitude-profile for three different power-law fluids are given in figure 4.6. Note that these non-dimensional calculations were independent of K_m, as the non-dimensional rheology was defined without K_m in equation 3.15. This enabled the research of the mere effect of the power index m on the steepness of decay. Note that the steepness of decay serves as a measure for the minimum required plate length of the waveguide. It was found that the amplitude-decay is overall steeper for smaller values of m (shear-thinning). At first sight this was an unexpected result, as it was presumed to be the opposite, based on the notice that the effective viscosity of a shear-thickening fluid increases while velocity gradients increase, thus accounting for a higher amount of viscous dissipation. The contradictory findings can be explained by looking at the (non-dimensional) effective viscosity of a shear-thinning and shear-thickening fluid. In figure 4.7 the dimensionless rheologies for fluids with $m = 0.5, m = 1$ and $m = 1.5$ are plotted. Note that in this computational experiment, the shear-rate $|d\hat{v}/d\hat{y}|$ stays below a critical value at which the lines would cross. Thus in this specific experiment, the shear-stress of the shear-thinning fluid is at all times higher than for the shear-thickening fluid at the same shear rates. The same finding is illustrated in figure 4.8. In these plots the dimensionless shear-rate over time is compared to the effective viscosity, for two fluids with $m = 0.5$ and $m = 1.5$. Note that this plot is in line with figure 4.7, as it can be observed that the amplitude of the effective viscosity for shear-thinning is higher than the amplitude for shear-thickening. This now concludes the cause for the steeper amplitude-decay for shear-thinning fluids in this experiment, when leaving the influence of K_m out of notice.

In figure 4.9 the dimensional results for the amplitude-profile for three different power-law fluids are depicted. It can be observed that the decay-length over z varies greatly for the different fluids.

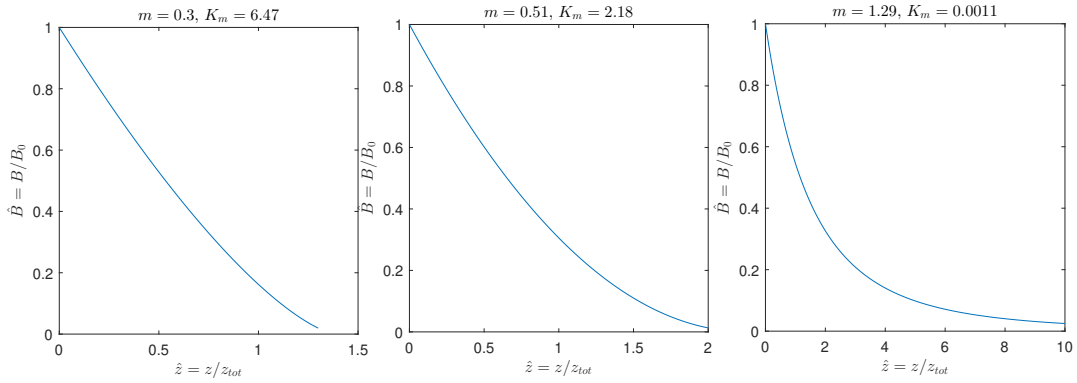

Figure 4.6: Plots of non-dimensional amplitude profile $\hat{B}(\hat{z})$ for three different power-law fluids (from left to right: ketchup, soybean oil, ethylene-glycol).

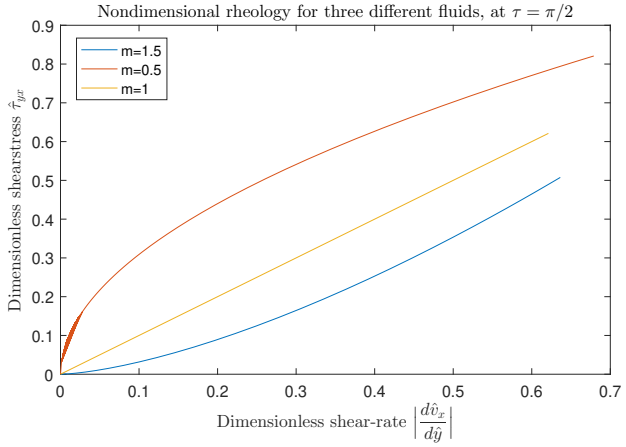

Figure 4.7: Non-dimensional rheology plot for power-law fluids with $m = 0.5$, $m = 1$ and $m = 1.5$.

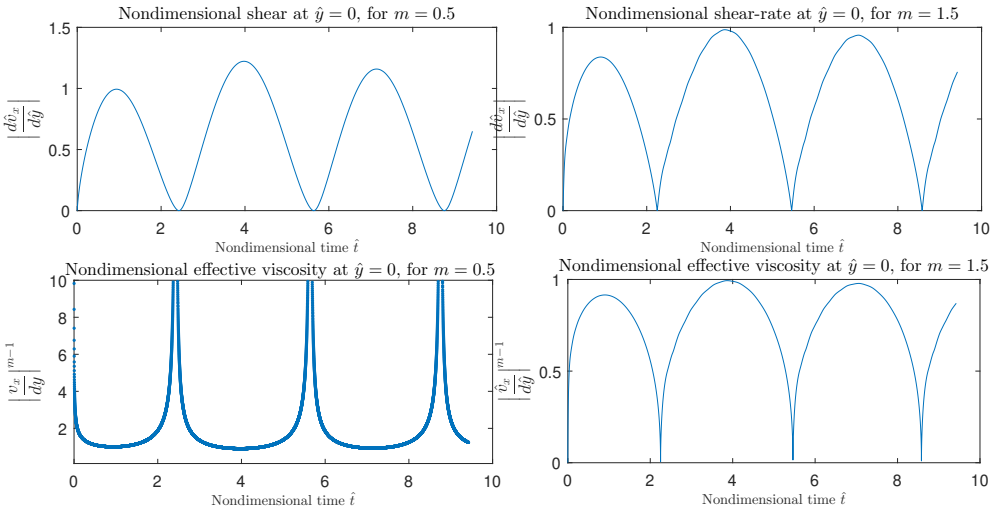

Figure 4.8: Plots of the non-dimensional shear-rate and effective viscosity at the plate's surface $\hat{y}$, for a shear-thinning ($m = 0.5$) and shear-thickening ($m = 1.5$) fluid. As an illustration for the steeper amplitude decay for shear-thinning fluids. Note that the effective viscosity diagram for $m = 0.5$ (bottom-left) blows up when the shear-rate tends to zero. This is a drawback of the power-law model, as was earlier described in section 2.1.

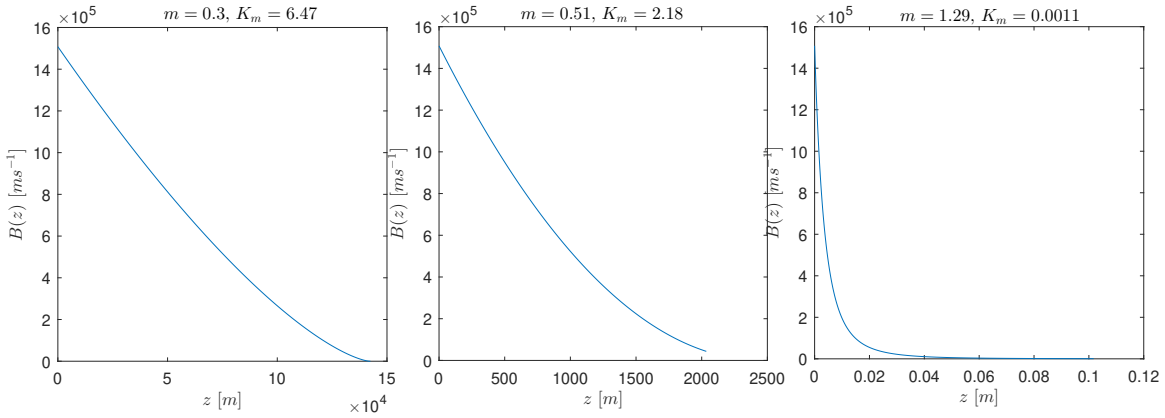

Figure 4.9: Plots of dimensional amplitude profile $B(z)$ for three different power-law fluids (from left to right: ketchup, soybean oil, ethylene-glycol). The total length of the waveguide in the experiment is $z = 204mm$.

As these amplitude plots are calculated using a dimensional velocity model, K_m plays a role in the pace of decay. That is, a higher K_m accounts for a higher shear-stress, a higher amount of viscous dissipation and thus a steeper decay. As it was beyond the scope of this thesis, it is recommended to research the effect of the consistency index K_m on the required plate length in the experiment.

4.3 Viscosity of the Newtonian fluids

As by the methods described in sections 3.4.1 and 3.5.5, the viscosity of the Newtonian fluids can be retrieved from the computed amplitude profile by performing an exponential fit. The resulting viscosities for the two Newtonian fluids water and air are given in table 4.1.

Fluid	**μ, non-dimensional calc**	**Deviation**	**μ, dimensional calc**	**Deviation**
Water	0.0010	0%	0.0010	0%
Air	1.8921e-05	3.4%	1.9025e-05	4.0%

Table 4.1: Resulting viscosities μ $[Pas]$ for two Newtonian fluids, compared to their literature values (table 3.2). Viscosity-results were computed both non-dimensional and dimensional methods using resp. 3.32 and 3.33. Calculated viscosities have a 95% confidence bound.

As can be observed from the table, the calculated viscosities are conform the theoretical values within the 95% confidence bound. This makes that a final benchmark on the numerical model is performed. Namely, it can be concluded that the calculation of velocity profile and amplitude profile is correctly performed, and the methods can thus be expanded to power-law fluids.

4.4 K and m of the power-law fluids

For power-law fluids not one, but *two* parameters have to be measured in order to know the effective viscosity of the fluid. This computation was only performed in dimensional space. As by the methods described in sections 3.4.2 and 3.5.5, the rheological parameters m and K_m can be retrieved from a linear data-fit to the computed data-set $[z, B]$. The resulting rheological parameters for three different power-law fluids are given in table 4.2. These results and errors ϵ on m and K_m are discussed in sections 4.4.1 and 4.4.2, respectively.

4.4.1 Discussion m-determination

As can be observed in table 4.2, the determination of m proves to be quite accurate with the used linear method. The existing error ϵ_m originates from the grid-size of the m_{fit} that is used to find

Fluid	Result m	Lit. m	Result K_m	Lit. K_m
Tomato ketchup	0.2997	0.30	66.5368	6.47
Soybean oil	0.5080	0.51	33.238	2.18
Ethylene-glycol	1.2943	1.29	7.8003e-7	0.0011

Table 4.2: Resulting power indexes m $[-]$ and consistency indexes K_m $[Pas^m]$ for three power-law fluids, compared to the inserted literature values.

the best linear fit to $[\Delta B^*, \Delta z^*]$. This linear fitting was performed by using an evenly spaced vector $m_{fit} = [0.1, 1.8]$ with $\Delta m = 0.0043$, hence $\epsilon(m) = 0.0043$. Note that the errors in the computed m-values for the three different values indeed lie in this margin.

A critical remark is to be expressed on an interesting phenomenon that occurred in the determination of m. As described in the experimental method 3.4.2, m is found by performing a minimization problem to $\epsilon_{y_{fit}} \to 0$. Interestingly, it was observed that $\epsilon_{y_{fit}}$ approaches zero at *two* values of m_{fit}, instead of just at *one*. An illustration of this phenomenon is given in figure 4.10.

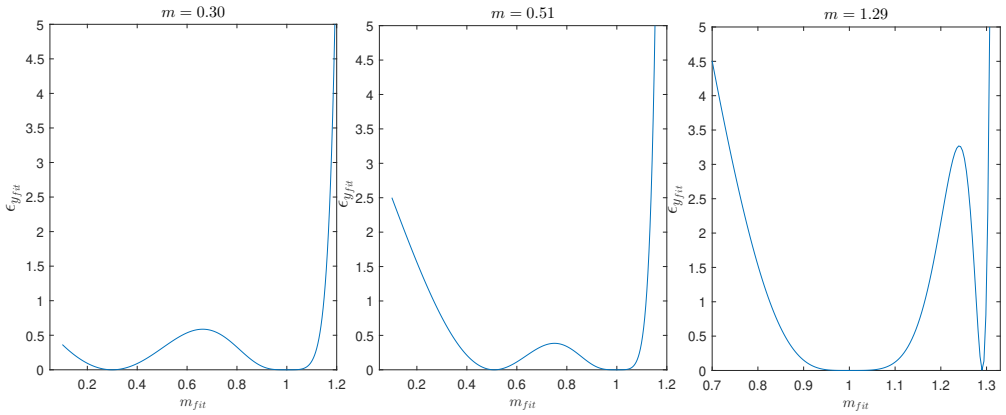

Figure 4.10: Illustration of the two-minima-problem in the minimization of the fit-error $\epsilon_{y_{fit}}$. The plots show a snapshot of $\epsilon_{y_{fit}}$ as a function of m_{fit}, for three different fluids (left to right: ketchup, soybean oil and ethylene-glycol).

As can be observed, the faulty minimum appeared around $m = 1$ in all examined cases. From this observation, it was hypothesized that for shear-thinning fluids the *first* dip in this plot indicates the correct m-value, as for shear-thickening fluids the *second* dip marks the right m-value. The use of this *two-minima-hypothesis* enabled the correct retrievement of m-values for the three tested fluids. A possible cause of this phenomenon could lie in the used method of minimization, or in the overall method of linear fitting. As this lies beyond the scope of this research, it is recommended to perform further investigation on this phenomenon. It would be helpful to prove the hypothesis of the first/second-dip-minimization for shear-thinning and -thickening fluids.

4.4.2 Discussion K_m-sensitivity

Unfortunately, the resulting values for K_m given in table 4.2 show a significant deviation from with the inserted literature values. This was expected to be caused by the high sensitivity of K_m for small variations in m_{fit}. Figure 4.11 illustrates this sensitivity, taking soybean oil as an example. The error ϵ_{K_m} in the resulting K_m-value was expected to be indicated by the error in m. That is, $\epsilon_{K_m} = K_{m,fit}(m-\epsilon_m) - K_{m,fit}(m+\epsilon_m)$, with $\epsilon_m = 0.0043$ (as described in section 4.4.1). However, figure 4.11 shows that the theoretical value of K_m does not lie in the stated error-interval of the fitted K_m, for the example of soybean oil. This indicates the presence of other error and sensitivity factors in the determination of K_m.

Some ideas can be proposed to perform a sensitivity investigation in further research. Namely, dK_m/dm as a of function m and K_m are of interest in this study, and can be used as a measure

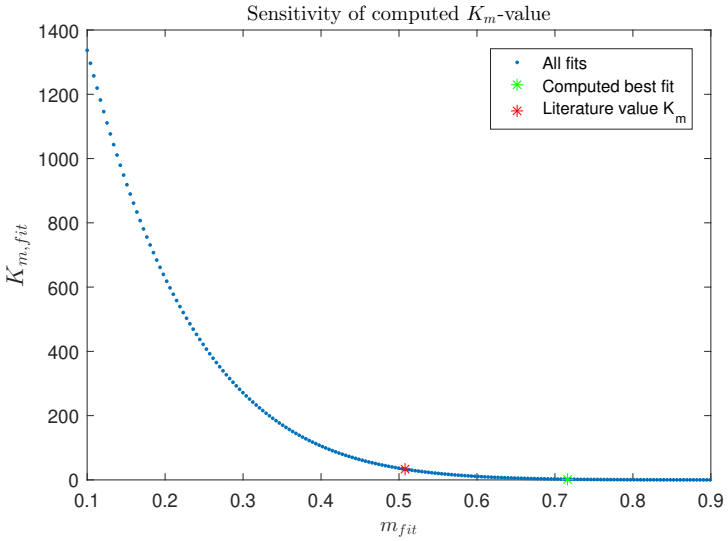

Figure 4.11: Snapshot of plot of the resulting consistency index $K_{m,fit}$ as a function of the fitted value of m_{fit}, for soybean oil with theoretical values $m = 0.51$ and $K_m = 2.18$. Giving an illustration of the sensitivity of K_m with regard to the 'choice' of m_{fit}.

for sensitivity. In other words: what is the sensitivity dK/dm when K_m is kept fixed, and m is perturbed a little? And vice versa? This calculation of dK_m/dm is proposed to be determined in the following ways:

1. Simulate the velocity profile, amplitude-decay and resulting $[K_m, m]$-fit for alternating m-values, keeping K_m fixed. Now the change in K_m for these different values of m gives the sensitivity with respect to m. And vice versa for K_m. This has the advantage that the simulation of the velocity profiles for different m-values is physically computed, and thus a physically accurate computation is performed. However the error in the fit is incorporated as well, which was seen in figure 4.11 to become quite large.

2. Plot the *analytical* derivative dK/dm (given in appendix **??**) of equation 3.34. Using the different data-set $B(z)$, calculated by the simulation of the velocity profile for different combinations of K_m and m. In this method, the computed dK/dm is independent of the errors in the fit of K_m and m.

Further computational research is required to investigate what method is most relevant and the least prone to fitting errors. Based on some limited research, two hypothesises are stated:

- $|dK_m/dm|$ decreases exponentially with m. This would indicate the experimental method of the rheology determination of power-law fluids to be more suitable for shear-thickening fluids.

- $|dm/dK_m|$ is independent of K_m. This would indicate the experimental method to have no restrictions on the value of K_m (plate-length considerations aside), as for every K_m the value of m could be retrieved without enlarging error.

Chapter 5

Conclusions and recommendations

In this thesis, a method to measure the rheological properties of power-law fluids with the ultrasonic viscometer was examined. In order to research this method accurately, a numerical model for the calculation of the calculation of the velocity- and amplitude-profiles for both Newtonian and power-law fluids was composed successfully. Based on these computations, the viscosity determination by methods of an exponential data-fit was tested successfully for two Newtonian fluids, water and air. This reaffirmed the ultrasonic waveguide experiment to be very applicable for Newtonian fluids. In the data-processing of the amplitude-profile for power-law fluids, the linear fitting method proved to be very accurate for the determination of power index m. The application of this method on the tested fluids ketchup ($m = 0.30$), soybean oil ($m = 0.51$) and ethylene-glycol ($m = 1.29$) resulted, respectively, the values $m = 0.2997$, $m = 0.5080$ and $m = 1.2943$, with $\epsilon_m = 0.0043$. However, it was found that the determination of K_m was not accurate with this method, as an error of more than 100% was found for all three tested power-law fluids.

Besides the main goal to determine the (effective) viscosity, much more insight was gained during this research. A much more efficient way of numerically calculating the amplitude attenuation by introducing X and I_X was developed. Furthermore, it was found that the viscous skin depth decreases with greater m and K_m. An unexpected result was the finding that the decay-length of amplitude $B(z)$ increased with m. This was attempted to be explained by looking at the shear-strain plot. This plot showed the velocity gradient in this particular set-up to stay smaller than a critical value, making that the shear-rate is overall lower for shear-thickening fluids. Resulting in the observation that the amplitude decay is less steep for higher m. For the experimental set-up, this means that a longer waveguide would have to be used for shear-thickening fluids.

Some recommendations for further research on the obtained results were stated. Firstly this is the dependence of the viscous skin depth, and the required plate length as a function of (m, K_m). This can be very useful for further development of the ultrasonic waveguide experiment set-up. Additionally, to improve the data-processing methods, the introduced hypothesis two-minima-problem needs to be studied, as well as the sensitivity dK_m/dm as a function of m_{fit}. Some ideas for this data-processing and sensitivity research were proposed in this thesis. Lastly, the numerical model could be further improved by studying the numerical stability criteria as a function of m.

This leads to the main conclusions of this thesis. That is, the proposed linear data-fitting method proposed by Rohde [15] is indicated to be useful for the determination of m. The method's accuracy has not yet shown to be high enough for the determination of K_m in this research.

Lastly, a general recommendation for further research is to expand the composed numerical model for complex rheologies other than the power-law rheology. The velocity- and amplitude-profiles can be computed directly with the numerical model composed in this thesis. Another data-processing method to retrieve the typical rheological parameters might have to be composed.

Bibliography

[1] Generation iv goals. https://www.gen-4.org/gif/jcms/c_9502/generation-iv-goals. Accessed: 2020-05-08.

[2] The concept of the molten salt fast reactor. http://samofar.eu/concept/. Accessed: 2020-30-06.

[3] Marc van den Berg. Viscosity determination using the quasi-scholte wave. Master's thesis, TU Delft, 2018.

[4] Transport phenomena in nuclear applications - concepts. https://www.martinrohde.nl/topics.html. Accessed: 2020-08-12.

[5] SI Cohen and TN Jones. Viscosity measurements on molten fluoride mixtures. Technical report, Oak Ridge National Lab., Tenn., 1957.

[6] S Cantor, WT Ward, and CT Moynihan. Viscosity and density in molten bef2–lif solutions. *The Journal of Chemical Physics*, 50(7):2874–2879, 1969.

[7] Remco Rook. Viscosity determination of newtonian fluids using shear ultrasonic guided wave attenuation. Master's thesis, TU Delft, March 2020.

[8] M Chrenkova, V Daněk, A Silnỳ, V Kremenetsky, and E Polyakov. Density and viscosity of the (lif[U+E5F8] naf[U+E5F8] kf) eut[U+E5F8] kbd4[U+E5F8] b2o3 melts. *Journal of molecular liquids*, 102(1-3):213–226, 2003.

[9] Alexander V Merzlyakov, Victor V Ignatiev, and Sergei S Abalin. Viscosity of molten lithium, thorium and beryllium fluorides mixtures. *Journal of nuclear materials*, 419(1-3):361–365, 2011.

[10] E Capelli, O Beneš, and RJM Konings. Thermodynamic assessment of the lif–thf4–puf3–uf4 system. *Journal of Nuclear Materials*, 462:43–53, 2015.

[11] Stanley Cantor. Density and viscosity of several molten fluoride mixtures. Technical report, Oak Ridge National Lab., Tenn.(USA), 1973.

[12] Alexander V Merzlyakov, Victor V Ignatiev, and Sergei S Abalin. Viscosity of molten lithium, thorium and beryllium fluorides mixtures. *Journal of nuclear materials*, 419(1-3):361–365, 2011.

[13] WP Mason, WO Baker, HJ McSkimin, and JH Heiss. Measurement of shear elasticity and viscosity of liquids at ultrasonic frequencies. *Physical Review*, 75(6):936, 1949.

[14] Thomas K Vogt, JS Lowe, and Peter Cawley. Measurement of the material properties of viscous liquids using ultrasonic guided waves. *IEEE transactions on ultrasonics, ferroelectrics, and frequency control*, 51(6):737–747, 2004.

[15] M. Rohde. M. rohde, determining the rheology of power law fluids with a wave guide at high-frequency shear waves, internal report. Technical report, Delft University of Technology,

2020.

[16] R.F. Mudde H.E.A van den Akker. *Fysische transportverschijnselen*. VSSD, TU Delft, 2013.

[17] L Ai and K Vafai. An investigation of stokes' second problem for non-newtonian fluids. *Numerical Heat Transfer, Part A*, 47(10):955–980, 2005.

[18] Francesco Rizzo, Fulvio Pinto, and Michele Meo. Investigation of silica-based shear thickening fluid in enhancing composite impact resistance. *Applied Composite Materials*, pages 1–21, 2020.

[19] Gualtiero Badin and Fulvio Crisciani. *Variational Formulation of Fluid and Geophysical Fluid Dynamics*. Springer, 2018.

[20] Corina Fetecau, D Vieru, and Constantin Fetecau. A note on the second problem of stokes for newtonian fluids. *International Journal of Non-Linear Mechanics*, 43(5):451–457, 2008.

[21] Hans Petter Langtangen and Geir K Pedersen. *Scaling of differential equations*. Springer Nature, 2016.

[22] David Pritchard, Catriona R McArdle, and Stephen K Wilson. The stokes boundary layer for a power-law fluid. *Journal of Non-Newtonian Fluid Mechanics*, 166(12-13):745–753, 2011.

[23] H.W. Hoogstraten. Collegedictaat toegepaste wiskunde ii, numerieke methoden. 1985.

[24] Deals Shaun Rikhotso. *Investigation of Stokes' second problem for non-Newtonian fluids*. PhD thesis, 2014.

[25] Léon Peter Bernard Marie Janssen and Marinus Maria Cornelis Gerardus Warmoeskerken. *Transport phenomena data companion*. Hodder Arnold, 1987.

[26] Vojtěch Kumbár, Sylvie Ondrušíková, and Šárka Nedomová. Rheological properties of tomato ketchup. *Potravinarstvo Slovak Journal of Food Sciences*, 13(1):730–734, 2019.

[27] Nelson Moraga, Alejandra Torres, Abel Guarda, and María José Galotto. Non-newtonian canned liquid food, unsteady fluid mechanics and heat transfer prediction for pasteurization and sterilization. *Journal of Food Process Engineering*, 34(6):2000–2025, 2011.

[28] Richard G Green and Richard G Griskey. Rheological behavior of dilatant (shear-thickening) fluids. part i. experimental and data. *Transactions of the Society of Rheology*, 12(1):13–25, 1968.

[29] Anthony Ralston and Philip Rabinowitz. *A first course in numerical analysis*. Courier Corporation, 2001.

Chapter 6

Appendix

6.1 Comments on non-dimensional derivations

All derivations on the non-dimensional quantities were performed with the aim of stating all governing equations in section 3.2.1 without constants. That is, in the 'most non-dimensional way possible', which enables the comparison of all computed results in terms of merely m, without interference of the K_m-value.

However, this approach was not completely correct. The non-dimensional differential equation 3.19 was verified by simply stating the definitions of $\hat{X}$ and $\hat{I}_{\hat{X}}$ in equations 3.17 and 3.18, respectively. However, this was frankly not a rightful derivation, as it is not in line with the proposed non-dimensional quantities $\hat{t}$, $\hat{B}$, $\hat{y}$, $\hat{z}$ and $\hat{v}_x$. By deriving $\hat{I}_{\hat{X}}$ in the rightful way, through using these aforementioned five non-dimensional quantities, a correct non-dimensional statement of the differential equation for $\hat{B}(\hat{z})$ can be found. Which derivation is given in this appendix. However, this new formulation of the non-dimensional differential equation for $\hat{B}(\hat{z})$ was not used in this research, as its definition inconveniently includes both K_m and m.

However, the newly derived correct formulation of the non-dimensional differential equation was used in further viscosity calculations for Newtonian fluids. The derivation in this appendix gives rise to a new formulation of $\hat{z}$, which then leads to a relation between $\hat{\alpha}_{fit}$ and μ.

Concluding, this appendix aims to point out the incongruity of the non-dimensional derivations in this thesis. For the calculation of the amplitude profile $\hat{B}(\hat{z})$, all non-dimensional quantities as stated in the main report were used. However, for the retrievement of the viscosity for Newtonian fluids, the derivation as given in this appendix was used, which is mainly based on a new formulation for $\hat{I}_{\hat{X}}$ and $\hat{z}$. Note that interestingly, despite of these two different non-dimensional methods being used simultaneously, the non-dimensionally retrieved viscosity results were still very accurate (see table 4.1).

6.1.1 Derivation non-dimensional differential amplitude equation

Substituting the non-dimensional formulations $\hat{B}$, $\hat{\tau}$ and $\hat{v}$ in the definition of $\hat{X}$ (3.17) gives:

$$\hat{X} = K_m^{-1} \left(\frac{\omega}{\nu_0 v_0^{m-1}} \right)^{-m/(m+1)} \cdot X. \tag{6.1}$$

Substituting equation 6.1 in the formulation for $\hat{I}_{\hat{X}}$ in 3.18 gives:

$$\hat{I}_{\hat{X}} = K_m^{-1} \left(\frac{\omega}{\nu_0 v_0^{m-1}} \right)^{-m/(m+1)} \cdot I_X. \tag{6.2}$$

Note that the non-dimensional formulation of $\hat{I}_{\hat{X}}$ in equation 6.2 is different than was stated in equation 3.13. The formulation of $\hat{I}_{\hat{X}}$ in 3.13 was just stated such that the simple differential

equation 3.19 could be stated, without any constants. However, when substituting equation 6.2 equation 3.19, this gives:

$$\frac{d\hat{B}(\hat{z})}{d\hat{z}} = v_0^{m-1} z_{tot} \cdot K_m \left(\frac{\omega}{\nu_0 v_0^{m-1}} \right)^{-m/(m+1)} \cdot \frac{1}{\rho_s c_s h} \hat{I}_{\hat{X}} \hat{B}(\hat{z})^m = C(m) \cdot \hat{I}_{\hat{X}} \hat{B}(\hat{z}). \tag{6.3}$$

Equation 6.3 shows the correct non-dimensional amplitude equation when following the five stated non-dimensional quantities. This is different with a factor $C(m, K_m)$ than the used differential equation in this research, being 3.19. Meaning that this factor $C(m)$ might have been ignored in calculations. It was simply assumed that the factor was insignificant, as the amplitude attenuation is relative in the end. However, this raises some questions, as it is not in line with the non-dimensional quantities.

6.1.2 Derivation non-dimensional $\hat{z}$

The newly derived non-dimensional formulation in equation 6.3 can be used to derive another formulation of $\hat{z}$, instead of $\hat{z} = z/z_{tot}$. Assuming that a non-dimensional formulation of $\hat{z}$ is not given, this gives: 6.2 and $\hat{B} = B/v_0$ into 3.4 gives:

$$\frac{d\hat{B}(z)}{dz} = v_0^{m-1} \cdot K_m \left(\frac{\omega}{\nu_0 v_0^{m-1}} \right)^{-m/(m+1)} \cdot \frac{1}{\rho_s c_s h} \hat{I}_{\hat{X}} \hat{B}(z) = C(m) \cdot \hat{I}_{\hat{X}} \hat{B}(z). \tag{6.4}$$

From equation 6.4 a new definition of $\hat{z}$ can be stated, being:

$$\hat{z} = \frac{v_0^{m-1} K_m^{-1}}{\rho_s c_s h} \left(\frac{\omega}{\nu_0 v_0^{m-1}} \right)^{-m/(m+1)} \cdot z. \tag{6.5}$$

This new definition of $\hat{z}$ again raises questions about the computed *non-dimensional* amplitude profiles for power-law fluids in this research, as the $\hat{z}$-axis would scale with different m according to this derivation.

6.1.3 Derivation viscosity retrievement Newtonian fluids

However, for Newtonian fluids the new derivation of $\hat{z}$ in equation 6.5 proves to be very useful. For $m = 1$ equation 6.5 reduces to:

$$\hat{z} = \frac{1}{\rho_s c_s h \mu} \left(\frac{\omega}{\nu_0} \right)^{-1/2} \cdot z. \tag{6.6}$$

Substituting equation 6.6 into the solution for $\hat{B}(\hat{z})$ in equation 2.18 gives:

$$B(z) = B(z) \exp\{(-\alpha \cdot z)\} = \exp\left\{ (\alpha \cdot \frac{\rho_s c_s h}{(\omega\nu_0)^{1/2} \rho_f} \cdot \hat{z} \right\} = \exp\left\{ (-(2\nu_0\rho_f)^{-1/2} \mu^{1/2} \cdot \hat{z}) \right\}. \tag{6.7}$$

Now it can be seen that a method of retrieving μ out of a non-dimensionally calculated amplitude-profile is found, as:

$$\hat{\alpha}_{fit} = -(2\nu_0\rho_f)^{-1/2} \mu^{1/2}, \tag{6.8}$$

which can be rewritten to

$$\mu = \hat{\alpha}_{fit}^2 \cdot 2\rho_f \nu_0. \tag{6.9}$$

Equation 6.9 was used in the calculation of the viscosity for Newtonian fluids out of the non-dimensionally calculated amplitude profile. This calculation was very accurate, the viscosities for water and air showed a deviation less than 5% (see table 4.1). This accuracy is very interesting, as it is suggested that different non-dimensional formulations are used simultaneously.

6.2 Derivative of K_m

Rewriting equation 3.34 in terms of K_m, and introducing $Y(m) = Y_a(m)/Y_b(m)$ for convenience, gives:

$$K_m = \left[\frac{\left| B(z)^{1-m} - B_0^{1-m} \right|}{\frac{2}{h\rho_s c_s} |1-m| P_3(m) (\omega\rho_f)^{m/2} \cdot z} \right]^{2/(2-m)} = \left[\frac{Y_a(m)}{Y_b(m)} \right]^{2/(2-m)} = Y(m)^{2/(2-m)}. \tag{6.10}$$

Deriving K_m in equation 6.10 to m gives:

$$\frac{dK_m}{dm} = \frac{2}{(2-m)^2} Y(m)^{-2/(m-2)} \ln\left(Y(m)\right) \cdot \frac{\frac{dY_a(m)}{dm} \cdot Y_b(m) - Y_a(m) \cdot \frac{dY_b(m)}{dm}}{Y_b(m)^2}, \tag{6.11}$$

in which

$$\frac{dY_a(m)}{dm} = \frac{(B(z)^{1-m} - B_0^{1-m}) \cdot (B_0^{1-m} \ln(B_0) - B(z)^{1-m} \ln(B(z)))}{\left| B(z)^{1-m} - B_0^{1-m} \right|}, \tag{6.12}$$

$$\frac{dY_b(m)}{dm} = \frac{2z(\omega\rho_f)^{m/2}}{h\rho_s c_s} \cdot \left(\frac{m-1}{|1-m|} P_3(m) + \frac{1}{2} |1-m| P_3(m) \ln(\omega\rho_f) + |1-m| \cdot \frac{dP_3(m)}{dm} \right). \tag{6.13}$$